Numerical Simulation of Two-Phase Flow in an Effervescent Atomizer for Nano-suspension Spray

Sanaz Arabzadeh Esfarjani

A Thesis

in

The Department

of

Mechanical and Industrial Engineering

Presented in Partial Fulfillment of the Requirements
for the Degree of Master of Applied Science (Mechanical Engineering) at
Concordia University
Montreal, Quebec, Canada

December 2007

Your file Votre référence
ISBN: 978-0-494-40907-7
Our file Notre référence
ISBN: 978-0-494-40907-7

NUMERICAL SIMULATION OF TWO-PHASE FLOW IN AN EFFERVESCENT ATOMIZER FOR NANO-SUSPENSION SPRAY

By

Sanaz Arabzadeh Esfarjani

ABSTRACT

Liquid atomization is widely used in industrial applications such as aerospace, combustion, pharmaceutical, spray coatings, and surface engineering. The main concern of atomization is to have a controllable and uniform spray. In suspension plasma spraying technique, where the attempt is to reach nano-scaled uniform coatings, there is a vital demand to produce a uniform and non-pulsating spray. Effervescent atomizers, in which a gas is bubbled into the bulk liquid through an aerator, have shown to be a technological alternative to the conventional atomizers when atomization of liquids with large variety of viscosity and density is required. Thus, understanding the behavior of gas and liquid flow through the nozzle is crucial to predict the condition of outcoming spray.

The objective of this study is to numerically investigate the two-phase flow inside the effervescent atomizers. Using the incompressible Eulerian/Eulerian approach, the three-dimensional structure of two-phase flow inside an aerated-liquid injector is modeled. The behavior of liquid film in the discharge passage is investigated using different Gas to Liquid mass flow Ratios (GLR). These numerical results are compared with the experimental data available in literature. The effect of nano-sized solid particles concentration on the liquid film thickness at the exit of the atomizer is studied through the change in liquid bulk density and viscosity.

Acknowledgements

I would like to express my gratitude to my supervisor Dr. Ali Dolatabadi for patiently guiding and constantly encouraging me through my study. He taught me what research is about and I will always be grateful to him for believing in me and supporting me during my work.

I would also like to thank Los Alamos National Laboratory (LANL) for providing us with the CFDLib code. This work is financially supported by Natural Sciences and Engineering Research Council of Canada (NSERC) and Le Fonds Québécois de la Recherche sur la Nature et les Technologies (FQRNT).

Table of Contents

List of Figures

Notations

A	total area
A_b	bubble projected area
A_k	cross-sectional area occupied by phase k
C	volume concentration of solid particles
C_D	drag coefficient
D	diameter
D_H	discharge passage hydraulic diameter
d_b	bubble diameter
$\vec{F}_{gl}$	momentum exchange force
$\vec{g}$	gravitational acceleration
GLR	Gas to Liquid mass flow Ratio
h	liquid film thickness
K_{gl}	momentum exchange coefficient
m	mass
$\hat{n}$	unit normal vector
p	pressure
p^*	face-centered equilibration pressure
Q	volumetric flow rate
Re	Reynolds number
S	control volume surface
t	time
$\vec{\vec{T}}$	total stress tensor
V	volume
X_k	phase indicator function

Greek letters

α	volume fraction
$\vec{v}_k$	velocity of phase k
$\vec{v}_k^*$	material velocity flux
υ_{gl}	kinematic viscosity of continuous phase
ϑ_k^0	microscopic specific volume
μ	viscosity
ρ	density
ρ_{gl}	density of continuous phase
ρ_k^0	material microscopic density
$\vec{\tau}$	shear stress tensor

Subscripts and superscripts

b	bubble
cv	control volume
g	gas
i,j,k	grid number
k	phase
L	Lagrangian
l	liquid
N	time step
p	solid particle
susp	suspension

1. Introduction

1.1 Motivation

Liquid atomization is a process of great importance in practical applications. The main purpose of atomization is to increase the specific surface area of a mass of liquid for better dispersion. Today, the liquid atomization, in which a liquid is dispersed as a stream of droplets, is found in many fields of applications such as aerospace, combustion, agriculture sprays, pharmaceutical industry and spray coatings and surface engineering. For instance, in diesel, spark ignition and gas turbine engines, the main purpose of atomization is to increase the specific surface area of liquid fuel in order to increase the rates of heat transfer, evaporation and mixing [1]. Similarly, in pharmaceutical industry for pulmonary delivery purposes, the goal of atomization is to produce a fine and uniform droplet sizes spray from the aqueous polymer solutions [2]. While, in spray coating and surface material application, it is attempted to spray the coating material as uniformly as possible in order to gain the coating with desired quality and characteristics.

One of the important applications of spray and atomization is in suspension plasma spraying [3,4,5]. Figure 1-1 shows a typical suspension plasma spraying system. In this new method of plasma spraying, the coating material in the form of powder with sizes, ranging from 30nm to 5μm is dissolved in a liquid carrier to form a suspension solution. The solution is then introduced into the plasma jet through an injection nozzle using a pressurized gas to shear the suspension and thus atomize it into a stream of fine droplets. Upon injection, in the plasma field where the temperature is in the order of 10,000 K, the carrier droplets containing the solid particles are vaporized and the small molten or semi molten solid particles are accelerated to hit the substrate and form the coating on the surface of the substrate.

One of the major advantages of suspension plasma spraying over conventional techniques is that by suspending powder in a fluid, feeding problems common in direct injection of solid powders are avoided [3,5] and it allows having a controlled injection of much finer particles than in conventional thermal spraying [5]. Hence, this method allows achieving thin and finely structured coatings with the thickness between few tens and few hundreds of micrometers. As a result, the final coatings have improved characteristics compared to those of conventional thermal spraying in the matter of having superior resistance to wear, erosion, cracking.

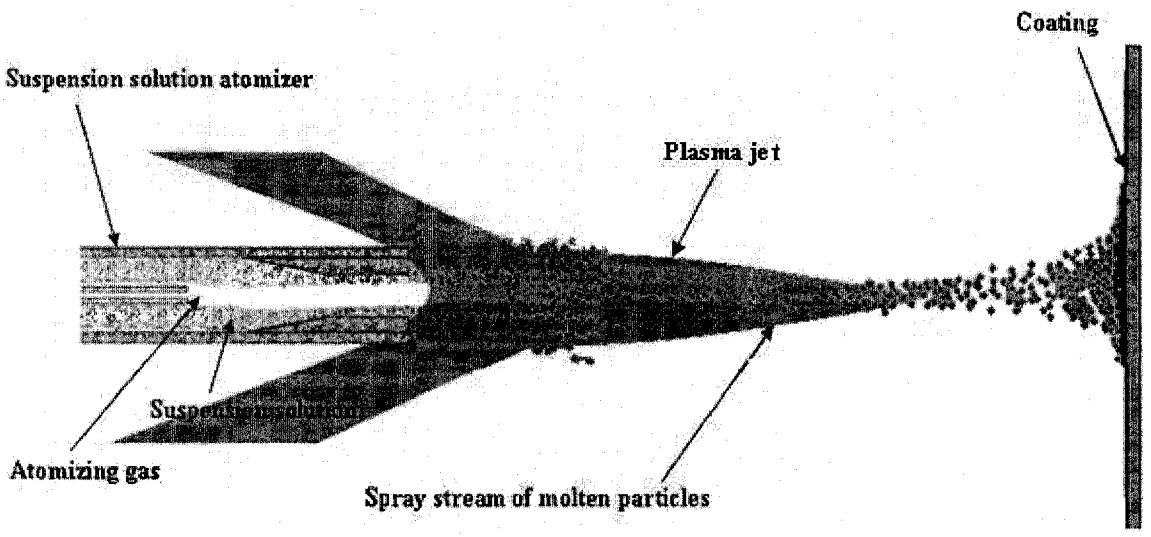

Figure 1-1 Schematic of suspension plasma spraying system

In a typical suspension plasma spraying, depending on the application, the concentration of suspended solid particles in liquid may vary from one case to another, thus the physical properties of the suspension solution does not remain unchanged. This will affect the characteristics of the spray and the distribution of the sprayed droplets in plasma field which subsequently influence the coating quality. Hence, one of the concerns about the spray systems in suspension plasma spraying is to have a controllable and repeatable spray flow for a wide range of operating conditions and various particle concentrations.

In current systems of suspension plasma spraying, mechanical injection is commonly used to spray and atomize the suspension solution [3,4,5]. It consists of injecting radially or axially of liquid jet with or without atomizing gas directly to the plasma jet. In most of the injection accompanied with the atomizing gas, the high speed atomizing gas perturbs the plasma jet and consequently causes the dispersed liquid droplets to detour the plasma

field [3,4]. Moreover, in conventional spray devices, the sprayed droplet size is highly dependent on the physical property of liquid. It is shown that the liquids with higher viscosity resist more to the dynamic force of atomizing gas [6]. These technical issues became as a motivation of this work to look for the possibility of a substitute for the atomizer system in suspension plasma spraying in order to have a more stable and repeatable spray process.

Through different mechanisms of liquid atomization, Aerated-liquid atomization, also called "effervescent atomization", is a technique that has so far been useful in a number of applications such as gas turbine combustors [7,8], internal combustion engines [9], furnaces and burners [10,11], and pharmaceutical sprays [2]. This method of atomization has been shown to produce well-atomized sprays with only a small amount of aerating gas at relatively low injection pressures [12]. It has been shown to work well even with liquids of high viscosity [11]. The detailed mechanism of effervescent atomizers is explained in the following section.

1.2 Effervescent Atomization

Work on effervescent atomization was first reported in the late 1980's by Lefebvre [12,13] and Roesler [14]. They introduced the technique of effervescent atomization in which a gas is bubbled into the bulk liquid through an aerator to form a bubbly two-phase mixture upstream of the final discharge orifice. Effervescent atomization is a method of twin-fluid atomization that involves the direct injection of gas into the liquid flow upstream of the injector exit [8,15].

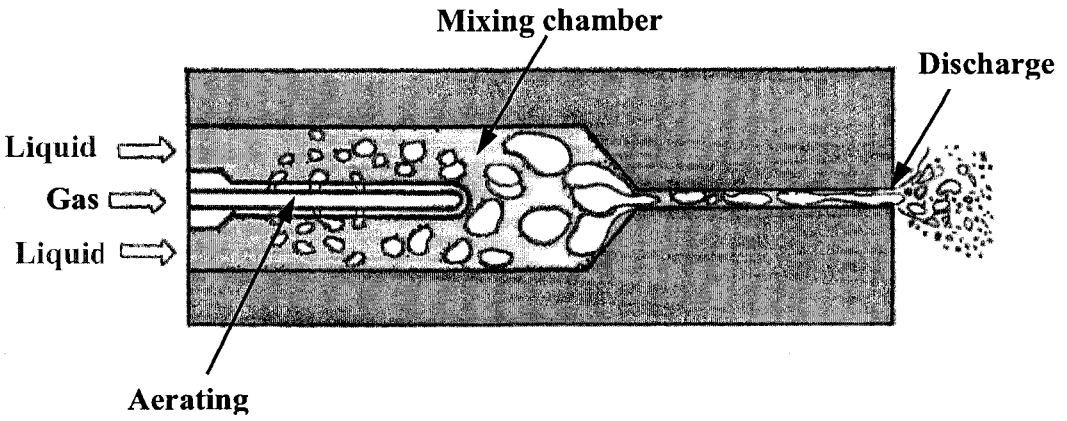

Figure 1-2. A schematic of typical inside-out effervescent atomizer (Tian 2002)

Effervescent atomizers are found in two different designs: inside-out and outside-in gas injection configurations, corresponding to how the gas is introduced into the liquid [8]. In both designs, the gas and the liquid are separately injected into a mixing chamber forming a two-phase gas-liquid flow in the nozzle. A typical inside-out effervescent atomizer is illustrated in Figure 1-2, consisting of four main components: liquid and gas supply ports, a mixing chamber where the gas is bubbled into the liquid stream, and an exit orifice. The gas – referred to as an 'atomizing gas' – is supplied to the mixing chamber by a central tube. At low aeration levels, the gas is bubbled into the liquid stream. The bubbly two-phase mixture flows thorough the nozzle and is ejected from the exit orifice. Upon exiting the atomizer, the bubbles burst and shatter the liquid into drops. In the outside-in atomizers, the atomizing gas enters the annular space surrounding the mixing tube and passes through small injection holes into the mixing tube to create a two-phase flow [15].

Several experimental studies have been carried out to determine the performance and spray characteristics of effervescent atomizers over wide ranges of operating conditions [16]. In this type of atomizers, better atomization quality can be achieved at injection pressures several times lower than those of conventional atomizers [7,12 ,13,14]. This would increase energy efficiency. Furthermore, the performance of effervescent atomizers is relatively insensitive to variations in liquid physical properties. This means that a single atomizer can handle a variety of liquids [17] and therefore it can be regarded as a positive feature for the suspension plasma spraying system where suspension solutions with various solid particle concentrations and materials are fed to the spray system.

The flow regime inside the nozzle has a great influence on the mechanism of spray and atomization process. The flow structure inside the orifice has a direct influence on the near-nozzle liquid break-up mechanism and is a key feature in determining the spray characteristics. Thus, understanding the behaviour of gas and liquid flow inside the nozzle is crucial to predict the liquid characteristics such as liquid film thickness close to the nozzle discharge orifice. The following section brings up the most important flow regimes that can occur inside effervescent atomizers.

1.2.1 Internal Two-Phase Flow Regimes

The spray characteristics in effervescent atomization are controlled by various variables through the two-phase flow inside and outside of the atomizer. The variables such as gas and liquid physical properties influence the flow inside the atomizer. The internal flow in turn, controls the external flow structure that determines the drop size and velocity through primary and secondary atomization. The internal flow in an effervescent atomizer

is more complex than in most single fluid atomizers. This is due to the fact that, such kinds of atomizers involve the internal mixing of the liquid with the atomizing gas and the evolution of the two-phase (i.e. gas-liquid mixture) as it flows through and out of the atomizer.

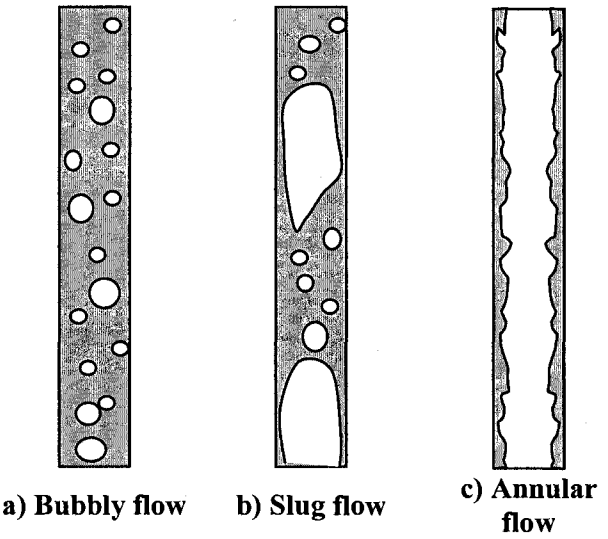

Figure 1-3 Internal two-phase flow regimes

Regarding the two phase flow regime inside a tube, depending on the distribution of the phases and the tube orientation, several flow regimes may exist. So far, there is no reliable theoretical model to predict the type of the flow pattern that occurs under any given set of operating conditions. The reason is that, the boundaries between the different flow regimes cannot be precisely defined since the transition from one flow pattern to another takes place slowly and depends on the observation and interpretation of the experimental data. Thus, the number of regimes and their characteristics are somewhat subjective and different investigators have identified different flow regimes for

geometrically similar flows. Therefore, the description and naming the various flow patterns is not completely unique and solid among different investigators [18,19].

The most important and noticeable flow regimes inside a pipe, as shown in Figure 1-3, can be defined as bubbly flow, slug flow, and annular flow. Figure 1-3a, shows the bubbly flow regime in which the gas phase is distributed more or less uniformly throughout the liquid phase in the form of discrete bubbles. In slug flow, Figure 1-3b, the two fluids redistribute themselves axially so that at any cross section, the flow rates of liquid and gas vary with time. The gas flows largely in the form of bubbles, which occupy most of the pipe's cross-sectional area and can vary in length, up to several times the pipe diameter. Successive bubbles are separated in the axial direction by liquid slugs that bridge the pipe and carry distributed bubbles. In annular flow regime, Figure 1-3c, the liquid flows as a thin wavy film along the walls of the pipe, while the gas flows in the core. The core may contain a large number of droplets that have been sheared from the wavy film.

Lörcher et al. [20] investigated the phase distribution at the effervescent nozzle exit and described its influence on the spray characteristics. They imaged the flow inside the nozzle with a high-speed camera. In their experiment, they could identify three flow regimes namely bubbly flow, slug flow and annular flow. They reported that only for bubbly and annular flows, there was a continuous spray flow, while for the slug flow the behavior of the generated spray was oscillatory. They worked with relatively high injection pressures within a range of 0.6 to 1.6 MPa.

Liquid break-up in effervescent atomization is initiated by aerodynamic shear forces generated by the injection of atomizing gas [21]. The principle of effervescent atomization has been investigated experimentally by different researches. Roesler and Lefebvre [14,22] conducted experiments to visualize both the two-phase flow inside an effervescent atomizer close to the exit orifice and the near-nozzle liquid break-up mechanism. They observed that the bubbly two-phase mixture formed in the mixing chamber evolves as it flows towards the nozzle exit and may be in either a bubbly or slug flow regime inside the discharge orifice. Different flow patterns inside the nozzle result in different mechanisms for the atomization process and also affect the spray characteristics. For instance, in a bubbly flow regime, the mechanism of liquid break-up relies on the bubble rupture phenomenon [18]. As shown schematically in Figure 1-4, leaving the orifice, the bubbles experience a sudden expansion and hence shatter the liquid into drops. The experiments of Buckner et al. [17,23] and Lund et al. [24,25] showed a similar mechanism of rapidly expanding bubble shattering the liquid into drops. They also investigated the flow regime where the liquid forms an annular sheet within the discharge orifice and subsequently breaks up into thin ligaments due to the rapidly expanding gas core.

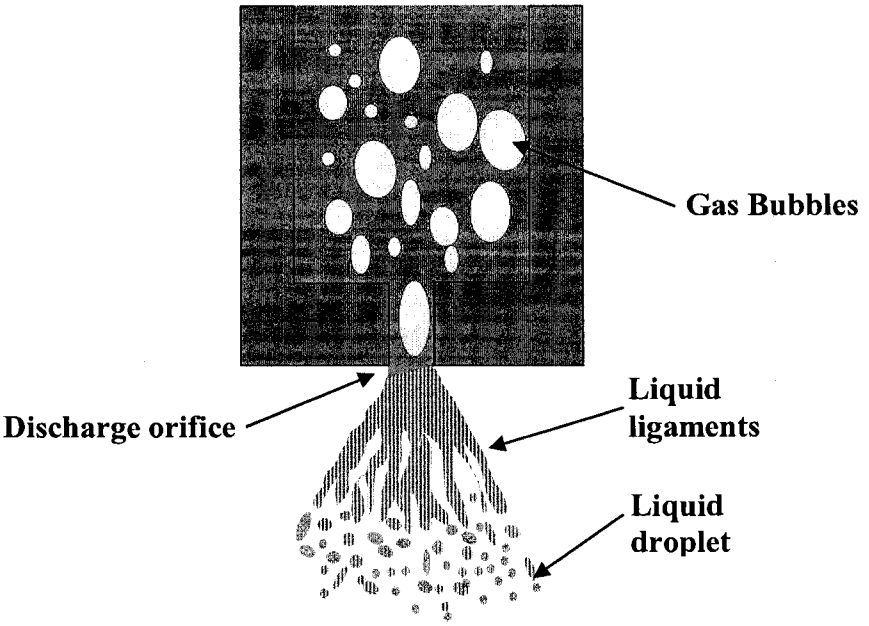

Figure 1-4. Effervescent atomization in bubbly flow regime

1.2.2 The Key Parameters in Effervescent Atomization

The spray characteristics can be defined as drop size and velocity distributions, spray cone angle, patternation (the radial and circumferential distribution of the liquid throughout the spray) and spray momentum flow rate. Generally, there are a large number of parameters related to the performance of the atomizer that influence the spray characteristics. These variables are classified by Sovani et al. [16] into categories as indicated by the boxes in Figure 1-5. These variables are explained below,

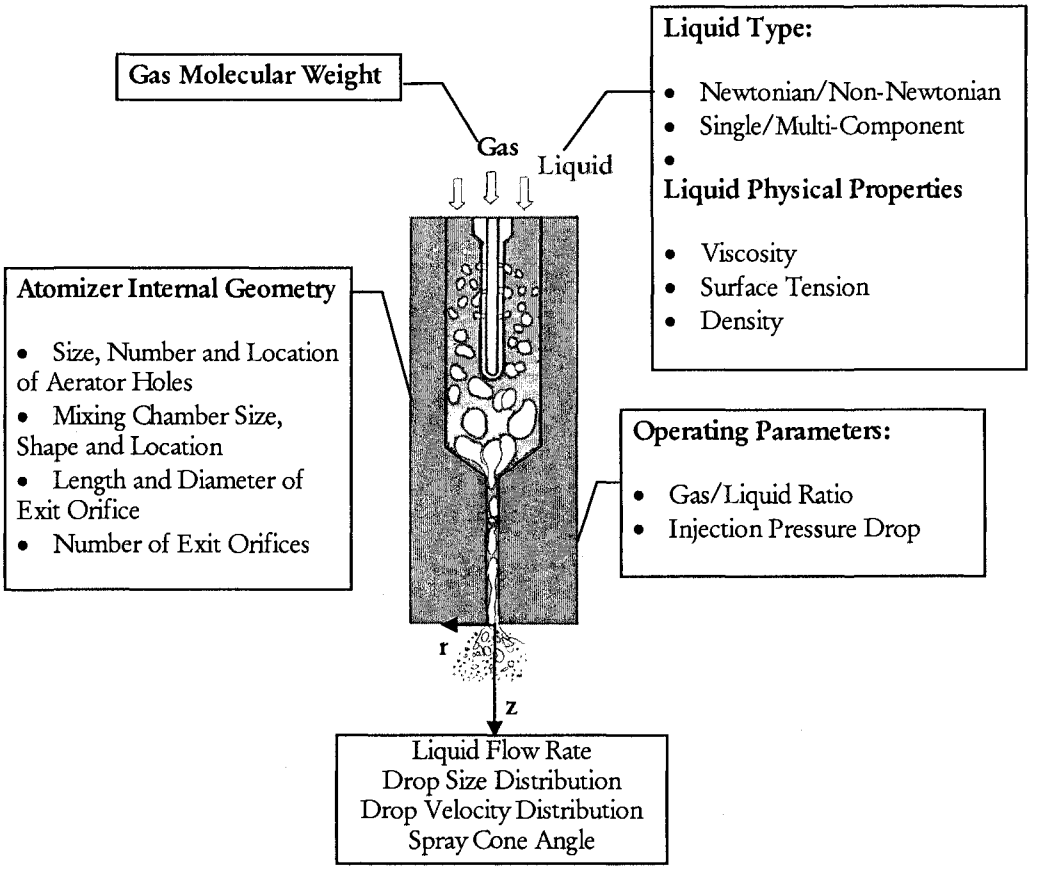

Figure 1-5 Some important variables in effervescent atomization

The Gas-to-Liquid mass flow Ratio (GLR): The Gas-to-Liquid mass flow Ratio (GLR) is an important operating parameter in most applications. In many applications, it is desirable to minimize the amount of atomizing gas while maintaining a small mean drop size. In general, most of the experimental works done on the effect of GLR, focused on the flow field outside and at the exit of the nozzle. The experimental data of Roesler and Lefebvre [14,22] and Li et al. [26] showed that as GLR is increased from zero to around 0.03, the mean drop size decreases rapidly and thereafter decreases at a slower rate with further increase in GLR.

Among the few works on the effect of GLR on two-phase flow inside the nozzle, Lin et al. [27] performed an experiment on the structure of the internal two-phase flow inside the aerated-liquid injector and the corresponding sprays under various aeration levels. In their experiment, they used five different types of aerating tubes, by varying the number and the place of holes on the aerating tube to provide various forms of gas injection inside the mixing chamber. For different gas-to-liquid mass flow ratios (GLR) and liquid flow rates, the liquid film thickness in the discharge passage was measured. They observed that the structure of the internal two-phase flow inside the discharge passage has a great influence on the resulting spray. By increasing the aerating gas flow, a co-annular flow structure was obtained in the discharge passage.

Roesler and Lefebvre [14,21] used high-speed photography to examine the flow patterns in the mixing chamber of an effervescent atomizer. The exterior surface of the atomizer was made of clear acrylic and glass to permit visual observation of the internal two-phase flow of air and water. From the analysis of photographs taken from the atomizer operating over wide ranges of pressure and GLRs, it was found that a bubbly flow can be maintained in the mixing chamber, upstream of the atomizer discharge orifice, only up to certain values of gas-liquid mass flow ratios. Further increase in the GLR causes the bubbles to grow in size and number until the flow pattern eventually becomes annular.

Influence of liquid physical properties: Several experimental studies have been conducted using a variety of liquids with different physical properties. Chin and Lefebvre [18] studied the effect of liquid viscosity and surface tension on flow patterns in the mixing chamber. In their experiment, they used a 25 mm mixing chamber with a 4.14mm-

diameter discharge orifice. They reported that the effect of surface tension is quite small, while, the general effect of an increase in liquid viscosity can result in separating the two flow phases more effectively. Lund et al [24] studied the effect of surface tension on sprayed droplet size, for an effervescent atomizer operating at mass flow rates of 1.5 g/s and below. They observed that at low aeration levels, the drop size decreases significantly with an increase in surface tension.

Regarding the studies on flow field outside the nozzle, the effect of changes in liquid viscosity on the variation of mean drop size was measured by Lund et al. [24], Sutherland et al.[28], and Buckner and Sojka [17]. They observed that the viscosity effect on the droplet size is rather small.

Patternation: The radial distribution of liquid mass within a spray is of importance in several areas. In combustion applications, local heat release rate and species concentration depend on the fuel radial distribution, while, for paint and spray coating of surface materials the radial liquid distribution determines both transfer efficiency and finish quality. Whitlow and Lefebvre [29] studied the radial liquid distribution in effervescent sprays for two values of GLR. The results indicate that the liquid mass flux initially increases with increasing the radial distance from the spray axis and reaches a maximum about half way between the spray axis and the outer edge of the spray and then decreases with further increase in radial distance. There are little or no information on the effect of liquid physical properties on the radial distribution of liquid mass in the spray produced by an effervescent atomizer.

Spray momentum flow rate: Spray momentum flow rate can be defined as the integral of liquid velocity squared times the liquid density over a specified area ($\int_A \rho_l (U_l)^2 \, dA$). This term determines the penetration distance of the spray. Momentum flow rates of sprays produced by the effervescent atomizer have been measured by Bush et al. [30], Sutherland et al. [31,32], Panchagnula and Sojka [33] at different injection pressures and GLRs. Their observations showed that spray momentum flow rate increases linearly with an increase in GLR, which they attribute to the higher discharge velocity of the gas phase produced by the increase in GLR.

The influence of liquid physical properties on spray momentum flow rate has been examined by Sutherland et al. [31,32].They found that spray momentum flow rate decreased slightly with an increase in liquid density. This was due to the decrease in liquid velocity that must occur if the density is increased and the liquid mass flow rate is held constant.

1.2.3 Suspension Effects on Effervescent Atomization

Regarding the suspension solution in aerated-liquid atomization, Schimdt et al. [34] presented measurements of velocity and flow pattern of a suspension in an internal twin-fluid atomizer at operating pressures ranging from 3 to 10 atm. They used a laser-sensor to determine the flow velocity and flow pattern at different operating conditions and positions inside the nozzle. They also studied the influence of various gas volume flow rates and particle concentration on the measured velocities and flow pattern inside the atomizer. They concluded that the spray velocity increases for higher gas volume flow rates, while higher particle concentrations have inverse effect and result in velocity

decrease. They observed two distinct flow regimes of slug and annular flow for low and high gas flow rates, respectively. Moreover, they did not observed any significant influence of the particle concentration on the flow pattern.

Generally, there is not much work reported on the flow regime and two-phase flow behavior inside the atomizer. This is due to the fact that the experimental investigation of two-phase flow in mini/micro orifices is technically and practically difficult. Therefore, the current understanding of effervescent atomization of internal flow is rather limited and topics such as the gas-liquid mixing phenomena inside the mixing chamber, evolution of the two-phase flow through the mixing chamber and the exit orifice are not fully understood. Hence, a numerical simulation which captures the physics of the two-phase flow, can be served as a tool to understand and analyze the flow field inside effervescent atomizers.

1.3 Two-Phase Flow Models

Two-phase liquid-gas models can be categorized in three classes: Inter-phase tracking, Eulerian/Lagrangian model and Eulerian/Eulerian models [35]. Inter-phase tracking models include the Volume of Fluid (VOF) and the level set models. They can track the position of the interface between the liquid and gas phases and give an accurate description of the place of the interface. However, these models are not able to solve a large number of bubbles. When the volume fraction of discrete phase compared to the continuous phase becomes considerable, these methods would results in enormous CPU time and storage requirements and almost become impractical. In the Eulerian/Lagrangian model, the liquid phase is treated as continuum in an Eulerian framework whereas the

bubbles (discrete phase) are tracked individually. In this model the computational cost increases with the number of bubbles. In Eulerian/Eulerian models, both phases are considered as inter-penetrating continuum [35], which means that at the same place both phases can exist, simultaneously. These models are feasible for any concentration of discrete phase and have no limitation on the number of bubbles. Therefore, they are suitable for two-phase gas-liquid flows which have a considerable amount of discrete phase (bubbles) inside the continuous phase (liquid). According to the level of mathematical complexity, the Eulerian/Eulerian models are classified to either mixture model or separated model (two-fluid model). The mixture model considers a single velocity (mixture velocity) for both phases and is limited to flows where the relative velocity between phases is negligible. While in the separated model the distinct properties of each phase as well as their relative distributions and interactions are taken into account and hence can be applied to a wider range of flow conditions.

Among a few numerical works done on modeling the two-phase flow inside the effervescent atomizers, the work of Tian [36] was on modeling the internal two-phase flow in the aerated-liquid injector configuration of the experimental work of Lin et al. [27]. The simulations were carried on for two different cases of (GLR) and compared with the experimental images. In his numerical simulations using a mixture model of two-phase flow, he captured and studied the time-dependent motion and growth of gas bubbles in the injector for two different low and high gas-to-liquid mass flow ratios. In his study, he idealized the injector to a two dimensional geometry. Arabzadeh and Dolatabadi [37,38,39] did 2D numerical simulations of the two-phase flow inside an

axisymmetric effervescent nozzle. They investigated the effects of the aeration level and solid particle concentration on the flow field inside the nozzle.

In this work an Eulerian/Eulerian model (i.e., two-fluid model) is used to numerically simulate the two-phase flow inside an effervescent atomizer.

1.4 Objectives

The objectives of this thesis can be summarized as follows:

- Numerically investigate the structure of the two-phase flow inside an effervescent atomizer using the Eulerian/Eulerian approach.
- Investigate the behaviour of liquid film in the discharge passage for different Gas to Liquid mass flow Ratios (GLR).
- Examine the effect of suspension solid particles through the liquid bulk density and viscosity on the two-phase flow at the exit cross section of the nozzle.

2. Numerical Methodology

2.1 Two Fluid Model

The two-fluid model is a proven approach to simulate two-phase flows. In the two-fluid model, in addition to separate sets of conservation equations for each phase, supplementary equations are considered that accounts for the interfacial transfer of mass, momentum, and energy between the phases. In any two-fluid system, volume fraction represents the volume occupied by a particular phase to the system's total volume. The two-phase problem in the present study consists of gas and liquid phases. Thus the volume fractions of gas and liquid phases are expressed as follows,

$$\alpha_g = \frac{V_g}{V} \tag{2.1}$$

$$\alpha_l = \frac{V_l}{V} \tag{2.2}$$

where V_g and V_l are the gas and liquid phase volumes, respectively and V is the total volume of the system.

2.2 Governing Equations

The two-fluid model is usually formed by applying an appropriate average to the local instantaneous conservation equations. For the incompressible, isothermal fluids considered in this study, one needs to only consider the conservation of mass and momentum within each phase along with the appropriate exchange term between the two phases. The conservation of mass and momentum equations for Newtonian, incompressible flow within each phase k are;

Conservation of mass

$$\frac{\partial \rho_k}{\partial t} + \nabla.\left(\rho_k \vec{v}_k\right) = 0 \tag{2.3}$$

Conservation of momentum

$$\frac{\partial\left(\rho_k \vec{v}_k\right)}{\partial t} + \nabla.\left(\rho_k \vec{v}_k \vec{v}_k\right) = \nabla.\vec{\vec{T}} + \rho_k \vec{g} \tag{2.4}$$

where $\vec{v}_k$ and ρ_k represent the velocity vector and density of phase k, respectively, $\vec{\vec{T}}$ is the stress tensor, expressed as: $\vec{\vec{T}} = -p\vec{\vec{I}} + \vec{\vec{\tau}}$ and $\vec{g}$ is the gravitational acceleration.

Averaging procedure

For a given point in a two-phase flow field, if the phase local instantaneous variables such as velocity were plotted as a function of time, it would fluctuate with sharp discontinuities occurring at phase interfaces. Most of the engineering analyses require only the mean values of macroscopic flow parameters. Hence, by averaging the local instantaneous governing equations, a set of averaged equations are derived that describes the mean dynamics of each phase.

In two-phase flow systems, various kinds of averaging have been defined and used. Among the different types of averaging, the time averaging, volume averaging, and ensemble averaging [40,41,42] are commonly used. Ensemble averaging which is used in this work is a general averaging case. It can be shown that both time and volume averages are special cases of the ensemble average [42].

Ensemble averaging of an arbitrary function, F, can be given as,

$$\bar{F} = \frac{1}{N}\sum_{n=1}^{N} F_n(\vec{x}, t) \tag{2.5}$$

where N represents the number of times the value of F is sampled at position $\vec{x}$ and time t. The averaging procedure will be assumed to satisfy the following relations.

Reynolds' rules:

$$\overline{f+g} = \bar{f} + \bar{g} \tag{2.6}$$

$$\overline{\bar{f} * g} = \bar{f} * \bar{g} \qquad \text{but} \tag{2.7}$$

$$\overline{f * g} \neq \overline{f} * \overline{g} \tag{2.8}$$

$$\overline{c} = c \qquad \text{where c is a constant} \tag{2.9}$$

Leibniz's rule:

$$\overline{\frac{\partial f}{\partial t}} = \frac{\partial \overline{f}}{\partial t} \tag{2.10}$$

Gauss's rule:

$$\overline{\nabla f} = \nabla \overline{f} \tag{2.11}$$

In order to distinguish between the phases during the averaging operation the phase indicator function, X_k, is used.

$$X_k(x,t) = \begin{cases} 1 & \text{if } x \text{ is in phase } k \text{ at time } t \\ 0 & \text{otherwise} \end{cases} \tag{2.12}$$

The volume fraction of phase k is defined as: $\alpha_k = \overline{X}_k$, (2.13)

Therefore we have: $\frac{\partial \alpha_k}{\partial t} = \overline{\frac{\partial X_k}{\partial t}}$ and $\nabla \alpha_k = \overline{\nabla X_k}$ (2.14,2.15)

The phasic average of a variable f is defined as: $\overline{f}_k^x = \frac{\overline{X_k f}}{\alpha_k}$ (2.16)

For the phase indicator function, X_k we have,

$$\frac{\partial X_k}{\partial t} + \vec{v}_k . \nabla X_k = 0 \tag{2.17}$$

The gradient of the phase indicator function, ∇X_k, is zero except at the interface. Therefore, it can be considered as delta-function for the phase interface.

2.2.1 Averaged Form of the Continuity Equation

The averaged equation of continuity is derived by multiplying the instantaneous conservation equations (2.3) by the phase indicator function for phase k, X_k, and then performing the averaging procedure.

$$\overline{\underbrace{X_k \frac{\partial \rho_k}{\partial t}}_{1} + \underbrace{X_k \nabla.\left(\rho_k \vec{v}_k\right)}_{2} = 0} \tag{2.18}$$

Using the product rule and performing the averaging process for each term specified by a number in the above equations, the conservation equations turns into the following form,

$$\underbrace{\overline{\frac{\partial\left(X_k \rho_k\right)}{\partial t}} - \overline{\frac{\rho_k \partial X_k}{\partial t}}}_{1} + \underbrace{\overline{\nabla.\left(X_k \rho_k \vec{v}_k\right) - \left(\rho_k \vec{v}_k\right) \cdot \nabla X_k}}_{2} = 0 \tag{2.19}$$

Multiplying the total derivative of X_k (i.e. equation (2.17)) by ρ_k, taking the average, and then subtracting from equation (2.19), one can derive the compact form of the averaged continuity equation,

$$\frac{\partial}{\partial t}\overline{\left(X_k \rho_k\right)} + \nabla \cdot \overline{\left(X_k \rho_k \vec{v}_k\right)} = 0 \tag{2.20}$$

Since the flow is incompressible in this work, the density of each phase will be constant through the averaging process. Therefore, the following relations hold for average density and velocity,

$$\frac{\overline{X_k \rho_k}}{\alpha_k} = \overline{\rho}_k = \rho_k^0 \tag{2.21}$$

$$\frac{\overline{X_k \rho_k \vec{v}_k}}{\alpha_k \overline{\rho}_k^x} = \frac{\overline{X_k \vec{v}_k}}{\alpha_k} = \overline{\vec{v}}_k \tag{2.22}$$

where ρ_k^0 is constant material (microscopic) density and $\overline{\vec{v}}_k$ is phasic averaged velocity. Substituting the above relations into (2.20), gives the continuity equation in terms of the average variables for each phase *k*,

$$\frac{\partial\left(\alpha_k \rho_k^0\right)}{\partial t} + \nabla \cdot \left(\alpha_k \rho_k^0 \overline{\vec{v}}_k\right) = 0 \tag{2.23}$$

Based on the incompressibility assumption, the continuity equation (2.23) reduces to the volume fraction transport equation,

$$\frac{\partial\left(\alpha_k\right)}{\partial t} + \nabla \cdot \left(\alpha_k \overline{\vec{v}_k}\right) = 0 \tag{2.24}$$

2.2.2 Averaged Form of the Momentum Equation

Similarly, the averaged momentum equation can be derived using the above procedure. In this case, the average of the total derivative of X_k, (i.e. equation (2.17)) is multiplied by $\rho_k \vec{v}_k$ and the result is subtracted from momentum equation (i.e. equation (2.4)). Using the proper average variables (cf. Appendix A), the final form of the averaged momentum equation is as follows,

$$\underbrace{\frac{\partial}{\partial t}\left(\alpha_k \rho_k^0 \overline{\vec{v}}_k\right)}_{(1)} + \underbrace{\nabla \cdot \left(\alpha_k \rho_k^0 \overline{\vec{v}}_k \overline{\vec{v}}_k\right)}_{(2)} = \underbrace{-\alpha_k \nabla \overline{p}}_{(3)} + \underbrace{\nabla \cdot \left[\alpha_k \left(\vec{\tau}_k - \vec{\tau}_k^{\mathrm{R\grave{a}}}\right)\right]}_{(4)} + \underbrace{\alpha_k \rho_k^0 \vec{g}}_{(5)} - \underbrace{\nabla\left[\alpha_k \left(\overline{p_k} - \overline{p}\right)\right]}_{(6)} + \underbrace{\left[\left(p - \overline{p}\right) I - \vec{\tau}\right]}_{(7)} \tag{2.25}$$

The terms in (2.25) are interpreted as follows;

(1) The local time rate of change of momentum for phase k per unit volume.

(2) The rate of convection of the momentum of phase k per unit volume.

(3) The contribution of the mean mixture pressure (i.e., equilibration pressure) to the force acting on phase k per unit volume.

(4) The k phase laminar (viscous) and turbulent Reynolds stress contribution to the force acting on phase k per unit volume. The turbulent part is not considered in this study.

(5) The gravitational body force acting on phase k per unit volume, which is negligible in this work.

(6) The acceleration by the non-equilibrium pressure. For the present two-fluid system of gas and liquid, it is negligible.

(7) The force acting on phase k due to the momentum exchange terms. This term accounts for the local pressure fluctuations and shear stress acting at the phase interface and is referred to as the averaged interfacial momentum exchange. In the next section 2.3, the model used to express this term in two-phase flow problems will be discussed.

For a two-phase or multiphase flow in addition to the above relations, the principle of continuity for n number of phases should be satisfied, i.e.,

$$\sum_{k=1}^{n} \alpha_k = 1 \tag{2.26}$$

2.3 Interfacial Momentum Exchange

Using the two-fluid model to solve two-phase problems requires additional information to complete the formulation and to describe the two-phase system entirely. Therefore, the supplemental information, such as equations of state, exchange terms between the phases, is needed as well as boundary and initial conditions.

The momentum exchange term in equation (2.25), namely term (7), represents a force per unit volume that is equal and opposite for the two materials in a two-fluid problem. The exact form of the force indicates that there are two main components. The first is a force due to pressure fluctuations, and the second is a viscous stress. Pressure fluctuations are created when there is a relative mean motion between the two phases.

Generally this term is referred to the averaged interfacial momentum exchange and includes the drag force and other transient forces. In modeling the interfacial momentum exchange source, it is assumed that this term can be expressed as a linear combination of the relations representing each physical force, such as drag, virtual mass, and buoyancy forces. Also, it is assumed that the transient effects of each force can be modeled by a linear combination of steady-state terms such as the standard drag coefficient [43]. In this study among various interfacial forces, the drag force has the most dominant effect.

Drag Force

In most cases, the drag force is an important component of the interfacial momentum exchange term. In most of the studies done in liquid-gas two-phase flows, the drag force is considered as a force exerted on a single spherical bubble moving in a continuous Newtonian fluid with a constant relative velocity. Therefore, the steady-state drag is defined as,

$$\vec{F}_D = -\frac{1}{2} C_D \rho_l \left|\overline{\vec{v}_l} - \overline{\vec{v}_g}\right| \left(\overline{\vec{v}_l} - \overline{\vec{v}_g}\right) A_b \tag{2.27}$$

where C_D is the drag coefficient, ρ_l the liquid density, A_b the bubble projected area and $\overline{\vec{v}_l}, \overline{\vec{v}_g}$ are the liquid and bubble velocities, respectively. Assuming the dispersed phase consists of uniform spherical bubbles with a diameter of d_b that occupies the total volume fraction of α_g, then the drag force on the bubbles per unit volume can be obtained,

$$\vec{F}_D = -\frac{1}{2}\left(\alpha_g \frac{\pi d_b^{\,2}/4}{4/3\pi(d_b/2)^3}\right) C_D \rho_l \left|\overline{\vec{v}_l} - \overline{\vec{v}_g}\right| \left(\overline{\vec{v}_l} - \overline{\vec{v}_g}\right) \tag{2.28}$$

which results in the following form,

$$\vec{F}_D = -\frac{3}{4}\frac{\alpha_g}{d_b} C_D \rho_l \left|\overline{\vec{v}_l} - \overline{\vec{v}_g}\right| \left(\overline{\vec{v}_l} - \overline{\vec{v}_g}\right) \tag{2.29}$$

In two-phase flow systems consisting of gas and liquid phases, the drag force can be expressed as follows,

$$\vec{F}_D = \alpha_g \alpha_l K_{gl} \left(\overline{\vec{v}_l} - \overline{\vec{v}_g}\right) \tag{2.30}$$

where α_l is the liquid volume fraction and K_{gl} is the momentum exchange coefficient, given by,

$$K_{gl} = \frac{3}{4}\rho_{gl} C_D \frac{\left|\vec{v}_l - \vec{v}_g\right|}{d_b} \tag{2.31}$$

As one can notice, the drag force in the two-phase flow consists of an exchange coefficient, multiplied by the product of the local volume fractions of each phase and relative velocity. The reason for utilizing this form will be explained in section 2.4.

The drag coefficient C_D used in equation (2.31) is the following correlation for steady-state drag between a spherical bubble and a Newtonian fluid [44],

$$C_D = 0.44 + \frac{24}{\mathrm{Re}_D} + \frac{6}{1+\sqrt{\mathrm{Re}_D}} \tag{2.32}$$

where,

$$\mathrm{Re}_D = \frac{\left|\vec{v}_g - \vec{v}_l\right| d_b}{\upsilon_{gl}} \tag{2.33}$$

In equations (2.31), (2.32) and (2.33) ρ_{gl} and υ_{gl} represent the density and kinematic viscosity of the continuous phase. Padial et al. [44] in their studies on the gas-liquid two-phase flow systems, made an empirical adjustment to the fluid density. In order to stabilize the gas-liquid interface and have a proper momentum exchange between the gas and liquid phases at both high and low gas volume fractions, they introduced a model for the fluid density used in equations (2.31), (2.32) and (2.33). By modifying the density of the continuous phase to change smoothly between the liquid density and the gas density,

the gas and liquid phases can equally change their role from dispersed phase to the continuous phase, when the flow regime is between or including either the two limiting cases of bubbles inside the liquid phase ($\alpha_g \to 0$), or the liquid droplets inside the gas stream ($\alpha_l \to 0$). The following modified correlation for the continuous-phase density of Padial et al. [44] is implemented in the current study,

$$\rho_{gl} = \frac{1}{2}\left\{\left(\rho_l + \rho_g\right) - \left(\rho_l - \rho_g\right)\tanh\left[\frac{2\left(\alpha_g - 1/2\right)}{\alpha_g\left(1-\alpha_g\right)}\right]\right\} \qquad 0 < \alpha_g < 1 \tag{2.34}$$

ρ_l and ρ_g are the material densities of the liquid and gas phases, respectively. Therefore, in equations (2.31), (2.32), and (2.33), ρ_{gl} is used instead of the single liquid density. As a result, the momentum exchange force can be expressed in momentum transport equation as follows,

$$\vec{F}_{gl} = \frac{3}{4}\frac{\alpha_g \alpha_l \rho_{gl}}{d_b}\left(0.44 + \frac{24}{\mathrm{Re}_D} + \frac{6}{1+\sqrt{\mathrm{Re}_D}}\right)\left|\vec{v}_l - \vec{v}_g\right|\left(\vec{v}_l - \vec{v}_g\right) \tag{2.35}$$

2.4 MFMAC Two-Fluid Numerical Technique

Kashiwa et al. [42] introduced a numerical method, for multiphase flow problems, which is an extension and generalization of the Implicit Continuous-fluid Eulerian (ICE) method. The ICE method is a finite volume scheme that is stable for any value of the Courant number based on the sound speed [42]. In the incompressible limit, the ICE

method reduces to the Marker and Cell (MAC) method [45]. In the new scheme of Multi-Fluid ICE method (MFICE), the more advanced multi-block integral with non-staggered mesh is used. This new approach has been shown to be both more robust and more general, which allows modeling of complex geometries. At the incompressible limit when all phases are incompressible, the MFICE scheme reduces to the MFMAC method.

The MFMAC method, used in the current study is from CFDLIB [46], a Los Alamos National Laboratory multiphase flow simulation code. It is an open source code which uses the Arbitrary-Lagrangian-Eulerian finite volume technique to integrate the time dependent multiphase governing equations. The code is based on the structured multi-block cell-centered solver. In this technique, depending on the level of complexity of the geometry, the computational domain is divided into simpler sub-domains, defined as blocks with structured grids in each block. Each interior face of a block is common between two neighboring blocks. In this method a single control volume is used for all conserved quantities (mass and momentum in this study), thus the fluid physical variables and properties such as velocity and pressure are located at the center of each mesh cell. In 2D problems, the control volume is an arbitrary quadrilateral and in 3D problems, is an arbitrary hexahedron. In the current analysis, the mesh is stationary throughout the calculation. A typical 3D cell with the cell faces and cell center arrangements is shown in Figure 2-1. In a structured mesh, since the neighboring cells have necessarily consecutive numbers, the localization of neighboring cells would be easier and faster in coding compared to the unstructured mesh configuration.

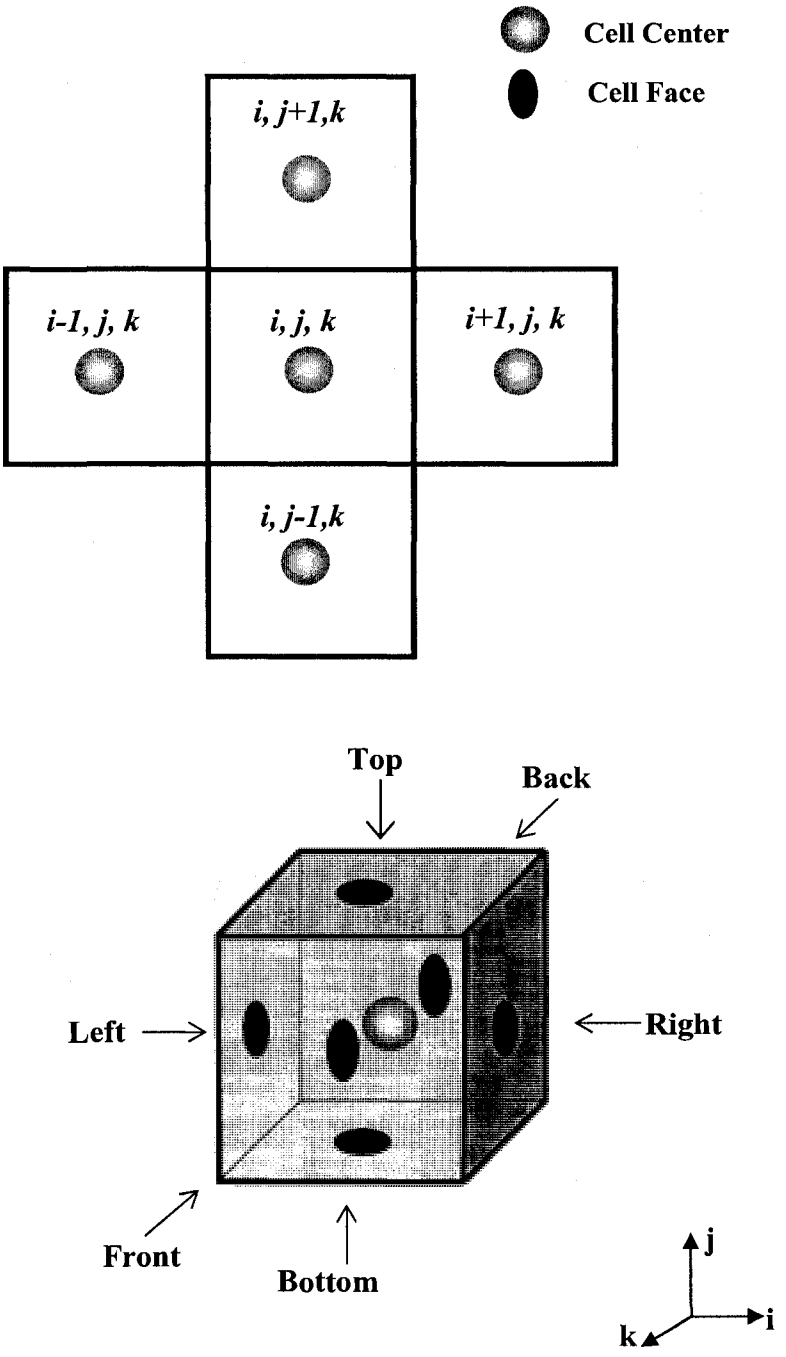

Figure 2-1 Grid arrangement and cell face labeling

The computational cycle can be divided into three main steps, namely,

1. ***The Primary Phase:*** includes the calculation of the auxiliary quantities
2. ***The Lagrangian Phase:*** takes into account the effects of physical processes
3. ***The Eulerian Phase:*** updates the state values for the new time level

If $q_k(\mathbf{x},t)$ is considered as a physical phasic property per unit volume, the relationship between the total change of q_k on the computational mesh to the change of q_k due to purely physical effects can be shown from the Reynolds Transport Theorem for a stationary computational mesh as follows [42],

$$\underbrace{\frac{d}{dt}\int_{V_k(t)} q_k dV}_{(1)} = \underbrace{\frac{\partial}{\partial t}\int_{V_{cv}(t)} q_k dV}_{(2)} + \underbrace{\int_{S_{cv}} q_k \vec{v}_k . \hat{\boldsymbol{n}}_{cv} dS}_{(3)} \tag{2.36}$$

where,

Term (1): The total changes in q_k due to the physical processes (Lagrangian change).

Term (2): The integral of the instantaneous change in q_k over the control volume at time t

Term (3): Advection of q_k out of the control volume due to the phasic velocity $\vec{v}_k$ at the surface $S(\mathbf{x},t)$. $\hat{\boldsymbol{n}}_{cv}$ is the outward normal vector of surface S.

Discretizing the above equation gives,

$$q_k^L V_k^L - q_k^n V^n = q_k^{n+1} V_{cv}^{n+1} - q_k^n V^n + \Delta t \mathcal{A}(q_k) \tag{2.37}$$

where superscripts n and $n+1$ represent the past and new time levels, respectively. The superscript L stands for Lagrangian solution. The reduced form of equation (2.37) is,

$$q_k^{n+1}V_{cv}^{n+1} = q_k^L V_k^L - \Delta t\,\mathcal{A}(q_k) \tag{2.38}$$

which is a relationship between the Eulerian $(n+1)$ and Lagrangian (L) portions of the solution. From the equation (2.38), it is apparent that in order to calculate the phasic property in the new time, q_k^{n+1}, both the Lagrangian volume, V_k^L, and the new mesh control volume, V_{cv}^{n+1}, must be determined. The values of these volumes can be obtained by applying the kinematic law for volume change. Hence,

$$V_{cv}^{n+1} = V^n + \Delta t \sum_{i=1}^{\substack{\#c.v \\ faces}} \left(S_i \hat{n}_i . \vec{v}_{mesh}\right) = V^n + 0 \tag{2.39}$$

$$V_k^L = V^n + \Delta t \sum_{i=1}^{\substack{\#c.v \\ faces}} \left(S_i \hat{n}_i . \vec{v}_k^*\right) \tag{2.40}$$

Since the computational mesh is not moving, $\vec{v}_{mesh} = 0$, the control volume will not change over time. From equation (2.40), the Lagrangian volume is equal to the material volume at time-level n, V^n plus the changes in volume due to the material velocity fluxes, $\vec{v}_k^*$, through the cell faces. It is the face centered fluxing velocity and represents the rate at which a volume of material k passes through the control volume surface i, (i.e. S_i). The

fluxing velocity will be calculated later in the Primary Phase Calculations section. It is the main result of the Primary phase.

The advection operator $\mathcal{A}(q_k)$ in (2.37) and (2.38) which stands for the control volume surface integral in (2.36) is discretized as follows,

$$\Delta t \mathcal{A}(q_k) = \sum_{i=1}^{\#c.v.\ faces} \Delta t S_i \hat{\boldsymbol{n}}_i . (\vec{v}_k^*)_i \left\langle \langle q_k \rangle \right\rangle_i^u \tag{2.41}$$

It is a sum over all surfaces defining the control volume, V^n, at time n. $\left\langle \langle q_k \rangle \right\rangle_i^u$ is an upwind-centered advected value of q_k, expanded in a spatial Taylor series, to a point, $\vec{x}$, just upstream of the cell face i [43],

$$\left\langle \langle q_k \rangle \right\rangle_i^u = \overline{q}_k + \nabla(q_k).(\vec{x} - \vec{x}_{upwind}) \tag{2.42}$$

where $\overline{q}_k$ is the cell averaged value of q_k, $\nabla(q_k)$ is an approximation to the gradient in the upstream control volume, $\vec{x}$ belongs to the upstream control volume and is a point between the upstream cell center and the cell surface and $\vec{x}_{upwind}$ is the cell center of upstream control volume.

If the phasic density and phasic momentum are substituted for the phasic properties per unit volume, q_k, the transport equations of mass and momentum will be obtained in equation (2.38).

Phasic Density Equation

Applying $q_k = \alpha_k \rho_k^0$ for phasic density parameter in equation (2.38) results in,

$$\left(\alpha_k \rho_k^0\right)^{n+1} V_{cv}^{n+1} = \left(\alpha_k \rho_k^0\right)^L V_k^L - \Delta t \mathcal{A}\left[\left(\alpha_k \rho_k^0\right)^n\right] \tag{2.43}$$

For the limit of incompressible flows the equation of phasic density reduces to the phasic volume fraction transport equation,

$$\left(\alpha_k\right)^{n+1} = \left\{\left(\alpha_k\right)^L V_k^L - \Delta t \mathcal{A}\left[\left(\alpha_k\right)^n\right]\right\} / V_{cv}^{n+1} \tag{2.44}$$

From the equation (2.44), to calculate the new phasic volume fraction, $\left(\alpha_k\right)^{n+1}$, in addition to the face centered fluxing velocity, $\vec{v}_k^*$, the Lagrangian value of phasic volume fraction , $\left(\alpha_k\right)^L$, should also be determined. This value is obtained by utilizing the definition of the Lagrangian term, from the left side of equations (2.36) and (2.37), as stated below,

$$\frac{\left(q_k^L V_k^L - q_k^n V^n\right)}{\Delta t} = \frac{d}{dt} \int_{V_k(t^n)} q_k dV \tag{2.45}$$

Hence, using the above relation for $q_k = \alpha_k \rho_k^0$ in combination with the continuity equation (2.24), yields the Lagrangian value of the phasic volume fraction,

$$\alpha_k^L = \alpha_k^n V^n / V_k^L \tag{2.46}$$

Phasic Momentum Equation

Using $q_k = \alpha_k \rho_k^0 \overline{\vec{v}_k}$ for phasic momentum parameter in equation (2.38) results in,

$$\left(\alpha_k \rho_k^0 \overline{\vec{v}_k}\right)^{n+1} V_{cv}^{n+1} = \left(\alpha_k \rho_k^0 \overline{\vec{v}_k}\right)^L V_k^L - \Delta t \mathcal{A}\left[\left(\alpha_k \rho_k^0 \overline{\vec{v}_k}\right)^n\right] \tag{2.47}$$

Similar to the phasic volume fraction equation, the Lagrangian value of phasic momentum, $\left(\alpha_k \rho_k^0 \overline{\vec{v}_k}\right)^L$, is determined using the equation (2.45) for $q_k = \alpha_k \rho_k^0 \overline{\vec{v}_k}$,

$$\frac{\left(\alpha_k \rho_k^0 \overline{\vec{v}_k}\right)^L V_k^L - \left(\alpha_k \rho_k^0 \overline{\vec{v}_k}\right)^n V_k^n}{\Delta t} = \int_{V_{cv}(t^n)} \left(RHS.\ Equation (2.25)\right) dV \tag{2.48}$$

The integral of the equation (2.48) is equal to the integral of the momentum equation's (2.25) right-hand side (RHS). The descritized form of the above equation for the Lagrangian phasic velocity, $(\overline{\vec{v}_k})^L$, yields an implicit relation due to the momentum exchange term,

$$\left(\overline{\vec{v}_k}\right)^L = \left(\overline{\vec{v}_k}\right)^n - \left(\frac{\Delta t}{\rho_k^0 V^n}\right) \sum_{i=1}^{\text{faces}}{}^{\text{\#c.v.}} \left(p^* \hat{n} S\right)_i + \left(\frac{\Delta t}{(\alpha_k \rho_k^0 V_k)^n}\right) \sum_{i=1}^{\text{faces}}{}^{\text{\#c.v.}} \left[\left\{\alpha_k \left(\overline{\overline{\tau}_k}\right)\right\}^n . \hat{n} S\right]_i + \left(\frac{\Delta t}{\rho_k^0}\right) \sum_{l \neq k}^{\text{\#Phases}} \left[\left(\alpha_l K_{kl}\right)^n \left(\overline{\vec{v}_l} - \overline{\vec{v}_k}\right)^L\right]_i \tag{2.49}$$

Now the reason for expressing the momentum exchange term as a product of the phases' volume fractions and a non-zero coefficient, mentioned in section 2.3 can be explained. For example, if phase one is vanishing (i.e., $\alpha_1 \to 0$) and phase two is appearing (i.e., $\alpha_2 = 1 - \alpha_1$), the velocity of phase two is unaffected by phase one and the exchange term in the momentum equation of phase two will be negligible. However, since the exchange coefficient K_{kl} is non-zero the exchange term for phase one will be nonzero, and phase one experiences velocity changes.

In the equation (2.49), p^* is the face centered equilibration pressure. Similar to the face-centered fluxing velocity, p^* is also determined in following section 2.4.1.

2.4.1 Primary Phase Calculation

The auxiliary terms which remain to be determined are the face-centered fluxing velocity, $\vec{v}_k^*$, and the face centered equilibration pressure, p^*.

Using the Lagrangian form of the conservative momentum equation, one can relate the face-centered fluxing velocity, $\vec{v}_k^*$, to the face-centered pressure gradient and the phasic momentum exchange term,

$$\frac{d}{dt}\left(m_k \vec{v}_k\right) = -\alpha_k V \nabla p + \sum_{l \neq k}^{\#\,\text{Phases}} \left[\alpha_k \alpha_l V K_{k,l}\left(\vec{v}_l - \vec{v}_k\right)\right] \tag{2.50}$$

It should be noted that the advanced time, t^{n+1}, is used in the above equation. Rewriting the equation in the descritized form yields,

$$\vec{v}_k^* = \left\langle\left\langle \vec{v}_k^n \right\rangle\right\rangle^{\rho_k} - \Delta t \left\langle\left\langle \vartheta_k^0 \right\rangle\right\rangle^{\rho_k} \nabla p^L + \Delta t \sum_{l \neq k}^{\#\,\text{Phase}} \left[\left\langle\left\langle \vartheta_k^0 \alpha_l K_{kl} \right\rangle\right\rangle^{\rho_k} \left(\vec{v}_l^* - \vec{v}_k^* \right) \right] \tag{2.51}$$

This equation is solved at the cell face and therefore the values of cell centered data at the right and left side of the cell face is utilized. In the above equation, the symbol, $\langle\langle\ \rangle\rangle^{\rho_k}$, represents the mass weighted average (cf. Appendix A), and ϑ_k^0 is the material microscopic specific volume ($=1/\rho_k^0$). The time advance pressure is approximated by p^L (the Lagrangian pressure). The approximate advanced time pressure p^L is splitted into the pressure value in the past time and the temporal change in pressure,

$$p^L = p^n + \Delta p \tag{2.52}$$

The exchange term is defined in terms of the phasic fluxing velocities $\vec{v}_k^*$ and $\vec{v}_l^*$ in advanced time level. From the implicit part of the fluxing velocity equation (2.51), it can be noted that the two phases are coupled implicitly through the momentum exchange term in the equation. In order to solve for $\vec{v}_k^*$, the fluxing velocity is decomposed into two parts, an explicit part, $\tilde{\vec{v}}_k$, and an implicit part, $\Delta \vec{v}_k^*$.

$$\vec{v}_k^* = \tilde{\vec{v}}_k + \Delta \vec{v}_k^* \tag{2.53}$$

where,

$$\begin{cases} \tilde{\tilde{\vec{v}}}_k = \left\langle\left\langle \vec{v}_k^{\,n} \right\rangle\right\rangle^{\rho_k} - \Delta t \left\langle\left\langle \mathcal{G}_k^0 \right\rangle\right\rangle^{\rho_k} \nabla p^n & (2.54) \\ \Delta \vec{v}_k^{\,*} = -\Delta t \left\langle\left\langle \mathcal{G}_k^0 \right\rangle\right\rangle^{\rho_k} \nabla(\Delta p) + \Delta t \sum_{l \neq k}^{\#\,\text{Phase}} \left[\left\langle\left\langle \mathcal{G}_k^0 \alpha_l K_{k,l} \right\rangle\right\rangle^{\rho_k} \left(\vec{v}_l^{\,*} - \vec{v}_k^{\,*} \right) \right] & (2.55) \end{cases}$$

Substituting the values of $\vec{v}_k^{\,*}$ and $\vec{v}_l^{\,*}$ into (2.54) results in the following linear system,

$$\begin{bmatrix} 1+\beta_1 & -\beta_1 \\ -\beta_2 & 1+\beta_2 \end{bmatrix} \begin{bmatrix} \Delta \vec{v}_1^{\,*} \\ \Delta \vec{v}_2^{\,*} \end{bmatrix} = \begin{bmatrix} \beta_1 \left(\tilde{\tilde{\vec{v}}}_2 - \tilde{\tilde{\vec{v}}}_1 \right) - \left\langle\left\langle \mathcal{G}_1^0 \right\rangle\right\rangle^{\rho_1} \Delta t \nabla(\Delta p) \\ \beta_2 \left(\tilde{\tilde{\vec{v}}}_1 - \tilde{\tilde{\vec{v}}}_2 \right) - \left\langle\left\langle \mathcal{G}_2^0 \right\rangle\right\rangle^{\rho_2} \Delta t \nabla(\Delta p) \end{bmatrix} \quad (2.56)$$

where $\beta_k = \left\langle\left\langle \mathcal{G}_k^0 \alpha_l K \right\rangle\right\rangle^{\rho_k}$.

Thus, the new fluxing velocity is expressed in terms of the past time values and the temporal change in pressure, Δp,

$$\vec{v}_k^{\,*} = \tilde{\tilde{\vec{v}}}_k + \begin{bmatrix} 1+\beta_1 & -\beta_1 \\ -\beta_2 & 1+\beta_2 \end{bmatrix}^{-1} \begin{bmatrix} \beta_1 \left(\tilde{\tilde{\vec{v}}}_2 - \tilde{\tilde{\vec{v}}}_1 \right) \\ \beta_2 \left(\tilde{\tilde{\vec{v}}}_1 - \tilde{\tilde{\vec{v}}}_2 \right) \end{bmatrix} - \begin{bmatrix} 1+\beta_1 & -\beta_1 \\ -\beta_2 & 1+\beta_2 \end{bmatrix}^{-1} \begin{bmatrix} \left\langle\left\langle \mathcal{G}_1^0 \right\rangle\right\rangle^{\rho_1} \\ \left\langle\left\langle \mathcal{G}_2^0 \right\rangle\right\rangle^{\rho_2} \end{bmatrix} \Delta t \nabla(\Delta p) \quad (2.57)$$

In order to calculate $\vec{v}_k^{\,*}$ and also p^L, the temporal change in pressure, Δp, should be calculated. Starting with the mixture continuity equation for incompressible two-phase flows, which is the sum of the phasic continuity equations of phases, and writing it for a typical control volume, results in,

$$\int_{V_{cv}} \frac{\partial \left(\sum_{k=1}^{\#\,\text{Phases}} \alpha_k \right)}{\partial t} dV + \int_{c.s.} \left[\sum_{k=1}^{\#\,\text{Phases}} \left(\alpha_k \overline{\vec{v}_k} \right) \right] . \hat{n}_{cv} dS = 0 \quad (2.58)$$

Equation (2.58) in the explicit form becomes,

$$V^n\Delta\left(\sum_{k=1}^{\#\text{ Phases}}\alpha_k\right)+\Delta t\sum_{i=1}^{\substack{\#\text{ c.v.}\\ \text{faces}}}\left\{S_i\hat{n}_i\left[\sum_{k=1}^{\#\text{ Phases}}\left(\vec{v}_k^{\,*}\left\langle\left\langle\alpha_k\right\rangle\right\rangle^u\right)\right]_i\right\}=0 \tag{2.59}$$

The term $\Delta\left(\sum_{k=1}^{\#\text{ Phases}}\alpha_k\right)$ should theoretically be zero, since $\sum_{k=1}^{\#\text{ Phases}}\alpha_k=1$, but in order to prevent the numerical errors, in practice this term is written as,

$$V^n\Delta\left(\sum_{k=1}^{\#\text{ Phases}}\alpha_k\right)=V^n relax\left(1-\sum_{k=1}^{\#\text{ Phases}}\left(\alpha_k\right)^n\right) \tag{2.60}$$

where *relax* is a relaxation factor which is typically set to 0.5 [43]. Finally, substituting the new fluxing velocity, $\vec{v}_k^{\,*}$, from equation (2.57) into (2.59), we reach the temporal change in pressure. This is the implementation of the Marker and Cell (MAC) method for multiphase flows.

$$-\left[\Delta t^2\sum_{i=1}^{\substack{\#\text{ c.v.}\\ \text{faces}}}\left\{S_i\hat{n}_i\left[\sum_{k=1}^{\#\text{ Phases}}\left(\vec{v}_k^{\,f}\left\langle\left\langle\alpha_k\right\rangle\right\rangle^u\right)\right]_i\right\}\right]\Delta p= \tag{2.61}$$

$$=-\Delta t\sum_{k=1}^{\#\text{ Phases}}\left\{S_i\hat{n}_i\left[\sum_{k=1}^{\substack{\#\text{ c.v.}\\ \text{faces}}}\left(\hat{\vec{v}}_k\left\langle\left\langle\alpha_k\right\rangle\right\rangle^u\right)\right]_i\right\}-V^n relax\left(1-\sum_{k=1}^{\#\text{ Phases}}\left(\alpha_k\right)^n\right)$$

where,

$$\vec{v}_k^{\,f} = \begin{bmatrix} 1+\beta_1 & -\beta_1 \\ -\beta_2 & 1+\beta_2 \end{bmatrix}^{-1} \begin{bmatrix} \langle\langle \vartheta_1^0 \rangle\rangle^{\rho_1} \\ \langle\langle \vartheta_2^0 \rangle\rangle^{\rho_2} \end{bmatrix} \tag{2.62}$$

$$\hat{\tilde{v}}_k = \tilde{\vec{v}}_k + \begin{bmatrix} 1+\beta_1 & -\beta_1 \\ -\beta_2 & 1+\beta_2 \end{bmatrix}^{-1} \begin{bmatrix} \beta_1\left(\tilde{\vec{v}}_2 - \tilde{\vec{v}}_1\right) \\ \beta_2\left(\tilde{\vec{v}}_1 - \tilde{\vec{v}}_2\right) \end{bmatrix} \tag{2.63}$$

The above system is nonlinear through the volume fraction advection term, $\langle\langle \alpha_k \rangle\rangle^u$. The value of this term depends on the fluxing velocity, $\vec{v}_k^*$ from equation(2.42), which in turn depends on Δp. Thus this is solved through iteration, during the solution of the linear system $\langle\langle \alpha_k \rangle\rangle^u$ is kept constant and updated during the outer (nonlinear iteration). A precondition conjugate gradient method is used to solve the linear system, for the outer (nonlinear) loop only a few iterations is needed. At the end of each nonlinear iteration the temporal change in pressure is used to update the new pressure, p^L, and hence to calculate the new value of $\vec{v}_k^*$. This new value of fluxing velocity is used to calculate the new value of $\langle\langle \alpha_k \rangle\rangle^u$. These new values are used into nonlinear iteration equation (2.61) and the process is repeated until the solution is converged, meaning $\Delta p \to 0$.

The last term needs to be found before the start of the Lagrangian-Eulerian part of the calculations, is the face-centered equilibration pressure, p^*. It is determined using a Total Variation Diminishing (TVD) scheme, in which p^* is written as the interfacial mixture mass weighted average of the cell-centered pressures, p^L, plus terms acting as filters to smooth the solution [42].

$$p^* = \left\langle\left\langle p^L \right\rangle\right\rangle^{\rho_{mix}} + \phi \frac{\sum\left[\left(\alpha_k \vec{v}_k\right)_r \left(\vec{v}_{k,r} - \vec{v}_k^*\right) - \left(\alpha_k \vec{v}_k\right)_l \left(\vec{v}_k^* - \vec{v}_{k,l}\right)\right]}{\sum\left[\left(\alpha_k \vec{v}_k\right)_r + \left(\alpha_k \vec{v}_k\right)_l\right]} \tag{2.64}$$

Where ϕ is the limiter term, that is designed such that $0 \le \phi \le 1$, with values tending toward zero if velocity field is smooth.

To summarize, the major numerical steps in the MFMAC code is as follows:

Primary Phase

- Evaluate the change in equilibration pressure Δp from equation (2.61)
- Back-substitute into equation (2.57) for $\vec{v}^*$, using p^L
- Evaluate the face-centered pressure p^* from equation (2.64)
- Evaluate the Lagrangian volume, V_k^L from equation (2.40)

⇓

Lagrangian Phase

- Evaluate the Lagrangian values, α_k^L and $\overline{\vec{v}}_k^L$ from equations (2.46) and (2.49)

⇓

Eulerian Phase

- Evaluate the time advanced values, α_k^{n+1} and $\overline{\vec{v}}_k^{n+1}$ from equations (2.44) and (2.47)

2.5 Geometry

The aerated-liquid injector geometry used in this work is similar to the one used in the experiments of Lin et al. [27] at the Air Force Research Laboratory (AFRL), Wright-Patterson Air Force Base. In their experiments, they used a rectangular aerated-liquid injector with transparent walls to visualize and measure the internal two-phase flow.

Figure 2-2 and Figure 2-3 show the 3-D view and the schematic cross-section of the injector in the x-y mid-plane (plane of symmetry), respectively.

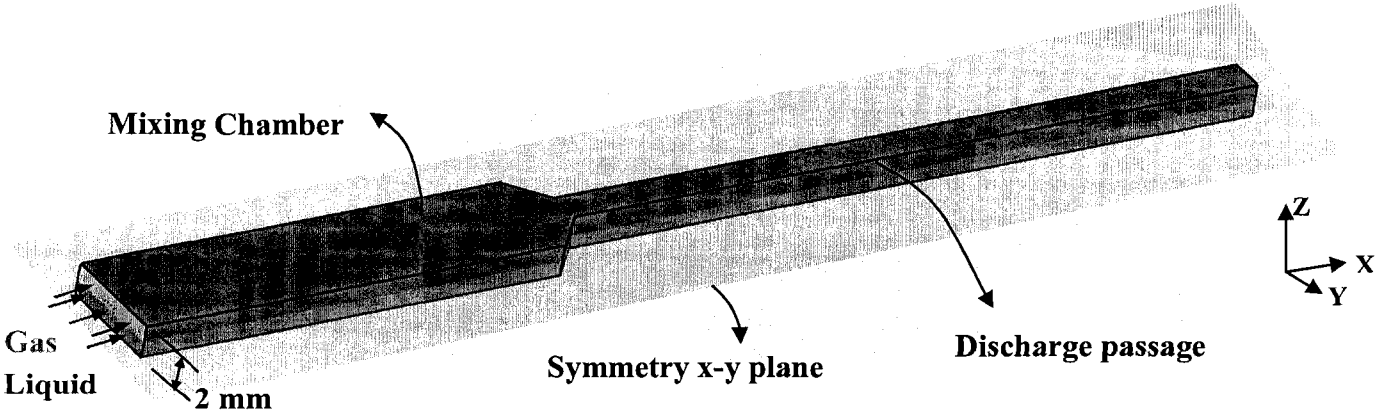

Figure 2-2 3D view of the injector with the symmetry mid-plane

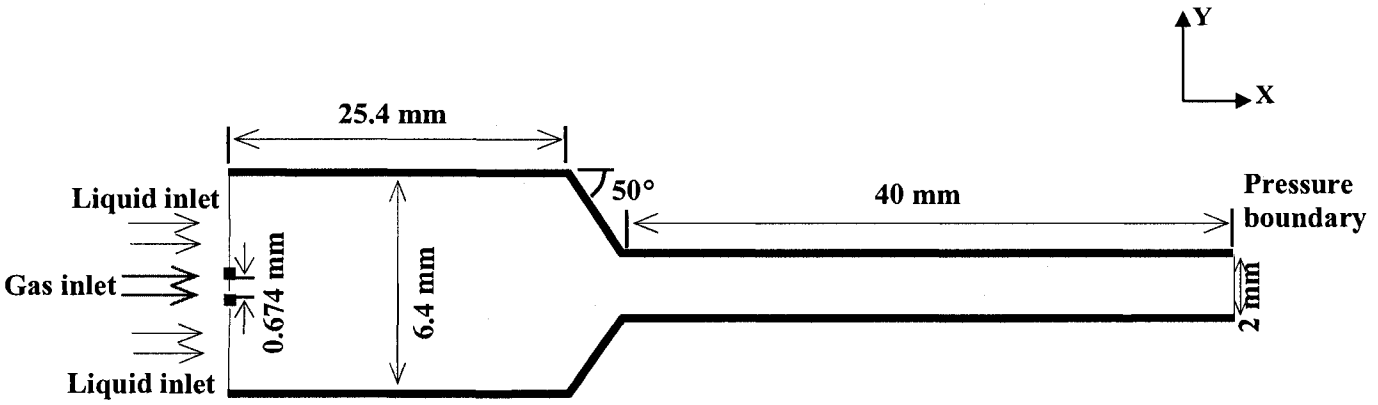

Figure 2-3 Schematic plan view of the injector cut through the mid-height (plane of symmetry)

This is a rectangular injector including the central injection of aerating gas flow. Lin et al. [27] showed that the central injection of gas generates more steady sprays with less pressure oscillation, compared to the radial gas injection. The reason for this is that in the case of peripheral injection, the aerating gas can impinge directly on the wall of the mixing chamber, causing both vibration of the injector body and the blockage of the liquid-phase mixture in the mixing chamber. This effect will be augmented for higher aeration levels.

As specified in Figure 2-3, the mixing chamber has the rectangular cross-section area with the dimension of 6.4 mm by 2.0 mm. The aerating gas is injected inside the liquid in the mixing chamber through a central 760 μm orifice which is located 25.4 mm from the entrance of the discharge passage. In order to make the geometry simple, the aerating orifice is assumed to have a square cross-section rather than a circular one with the corresponding dimension of 674 μm. The mixing chamber is connected to the discharge

passage through a converging part with an angle of 50°. The discharge passage has a square cross-sectional area with the dimension of 2 mm by 2 mm and the length of 40 mm.

2.6 Computational Domain and Mesh

In this study, since the geometry and flow is symmetry relative to the mid-plane (x-y plane of symmetry), only one half of the total domain in z direction is modeled. The reason for 3D simulation is to capture the asymmetric behavior and development of the gas phase inside the liquid phase based on different inlet gas flow rates which in turn, changes the liquid distribution inside the mixing chamber, the discharge passage and at the nozzle exit. These effects cannot be observed in 2D simulations [37,38,39].

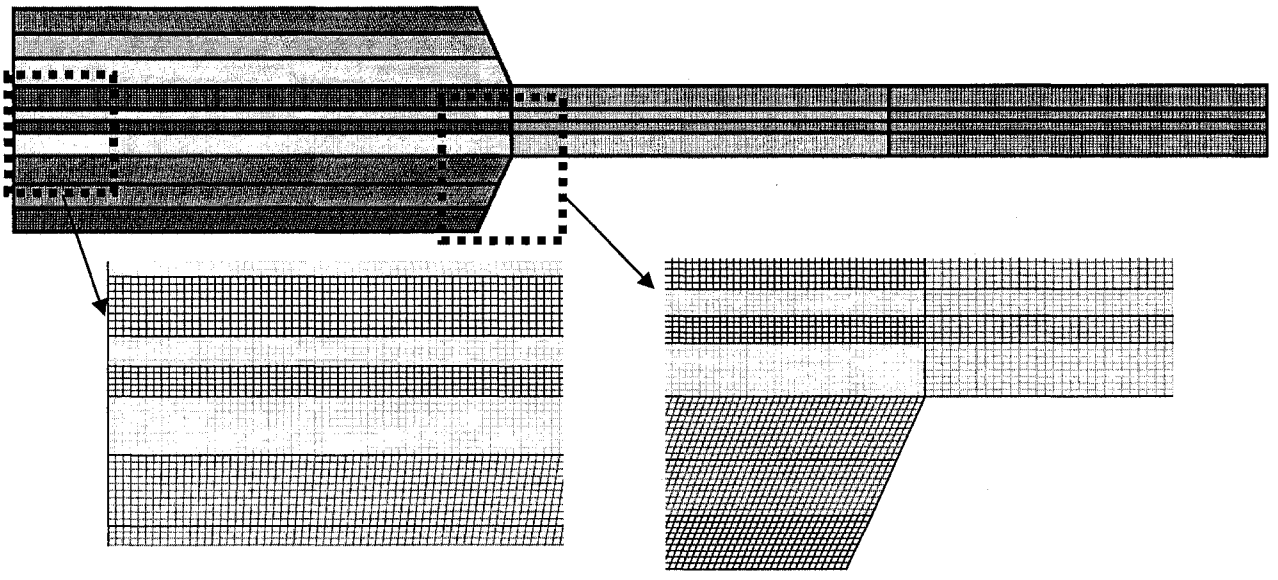

Figure 2-4 Computational blocks with corresponding mesh in plan view (x-y plane)

The computational domain is discretized by structured cubic cells as described in Section 2.4. The mesh created in this study has 36 blocks with the total number cells of 560,000. Figure 2-4 illustrates the computational blocks and the type of meshing that represents the nozzle geometry.

2.7 Boundary Conditions

Symmetric boundary condition is applied along the nozzle mid-plane (*x-y* symmetry plane). Both the liquid and gas inlets are modeled as velocity inlet boundaries and the volume fraction of each phase at the corresponding inlet, is set to be one. No-slip velocity condition at the nozzle walls is imposed. At the nozzle exit an outflow boundary condition with a pressure of 1 atm is applied.

Ethanol is used as the liquid and nitrogen is used as the aerating gas. Liquid is injected at a constant volumetric flow rate of 0.38 l/min as used in the experiments of Lin et al. [27]. Based on different gas-to-liquid mass ratios (GLR), different conditions for the gas volumetric flow rate are imposed in the aerating tube. These values are tabulated in Table 1.

GLR (%)	***Gas Flow Rate (l/min)***
0.08	0.18
0.15	0.34
0.19	0.42
0.30	0.74
0.50	1.15
0.80	1.85
1.25	2.80
1.80	4.15

Table 1 Inlet gas volumetric flow rate

The nozzle is initially filled with liquid and the two-phase simulation is started by introducing the gas phase inside the domain at a velocity based on a specific GLR.

2.8 Effect of Suspension

To model the suspension, the effect of nano-size particles on liquid phase was considered as the change in the liquid bulk density and viscosity. Suspension density is defined as [34];

$$\rho_{susp} = (1-C)\rho_l + C\rho_p \tag{2.65}$$

where ρ_l is the density of pure liquid, ρ_p is the density of solid particles_ in this study the glass particles are considered with density of 2500 kg/m^3_ and C is the volume concentration of solid particles in suspension. The most popular determination of the suspension viscosity, which takes into account not only the concentration of the solid phase, but also the interaction between the solid particles, is based on the well-known Thomas equation [47];

$$\mu_{susp} = \mu_l(1+2.5C+10.05C^2+0.00273e^{16.6C}) \tag{2.66}$$

The model considers that the flow is homogenous and is valid for the concentrations up to C=0.625 and particle size ranging from 0.099 to 435 μm. Since this study is mainly focused on nano-sized particles solution, the following relations are still valid, as the distribution of nanoparticles in liquid is more uniform and the solution is more homogenous than suspension solution of micron-sized particles. Due to the low concentration of solid particles in the liquid, the solution was treated as a homogeneous

Newtonian fluid. Therefore, the shear thinning behavior of the suspension which is significant in high solid concentrations is negligible.

Different particle concentrations were studied. By increasing the volume fraction of solid particles in the liquid from 0 to 0.192, the suspension density and dynamic viscosity increase up to 41.6% and 91%, respectively, compared to the case of pure liquid phase (Table 2).

Particles Volume Fractions	***% Increase in density*** ρ_{susp}	***% Increase in dynamic viscosity*** μ_{susp}
0.0	0.0	0.0
0.06	13.0	19.0
0.08	17.3	27.1
0.1	21.7	36.1
0.15	32.5	63.0
0.17	36.9	75.6
0.19	41.6	91.1

Table 2 Different solid particle concentration in the present study

3. Results and Discussions

In this section the results of the flow field simulation inside the aerated-liquid injector are presented. In all simulations, the volumetric flow rate of the liquid is kept constant at 0.38 l/min. In the first part, the volumetric flow rate of the gas phase is varied based on the various GLRs and the effect of the different aeration levels is investigated on the two-phase flow structure inside the mixing chamber and discharge passage. In the second part of the results, liquid with different particle concentrations_ based on the various liquid density and viscosities_ is injected to the nozzle and the effect of various particle concentrations is studied on the liquid film thickness emerging from the nozzle.

In the current simulations, the value used for the bubble diameter in the drag model, namely Equations (2.31) and (2.33), is based on the experimental work of Lin et al. [27]. In their experiment, they observed that for the case with the lowest GLR (0.08%) the separated bubbles were formed with diameters of 0.8-1.0 mm. Hence in the simulations, for the low GLRs such as 0.08%, bubbles with uniform size of 1 mm are considered.

While for the higher GLRs where practically there is no separated bubble in the liquid and there exists a continuous stream of gas, it is assumed that the drag force is simplified by a force applied from the large bubbles with diameter equal to the size of the exit orifice (2 mm).

3.1 The Effect of Aerating Gas (GLR)

Figure 3-1 presents the three dimensional view of the nozzle at three different level of aerations with the iso-surface of gas phase volume fraction of 0.5. As one can observe, at low GLR of 0.08%, Figure 3-1 a, the gas flow in mixing chamber is almost separated to relatively large bubbles. At this level of aeration, the gas flow has not enough energy to be dispersed throughout the mixing chamber and the effective mixing between the liquid and the gas phase is not significant. By increasing the aerating gas flow rate to GLR of 0.5%, Figure 3-1 b, instead of separate bubbles, a large plug of gas is developed inside the mixing chamber. The mixing level of gas flow with the liquid phase is still low. In the discharge passage, the slug flow generated from the entrance of the discharge passage, coalesce and form elongated gas slugs at the end of the passage. At the higher GLR of 1.25%, Figure 3-1 c, the dispersion of the gas flow is augmented. At this GLR, as the aerating gas reaches the nozzle walls, the geometry of the mixing chamber can have an effect on the way the gas flow expands and develops. Inside the discharge passage, a continuous stream of gas, in the middle of the passage is formed. This will result in a co-annular flow regime near the nozzle exit.

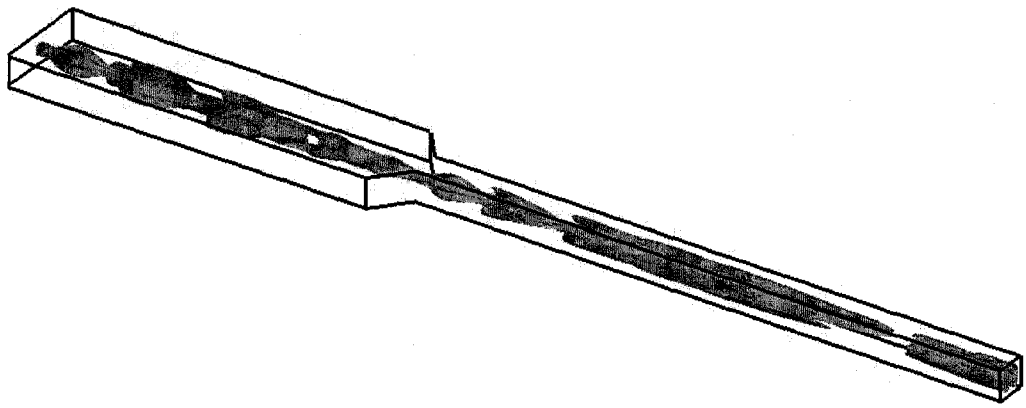

a) GLR 0.08%

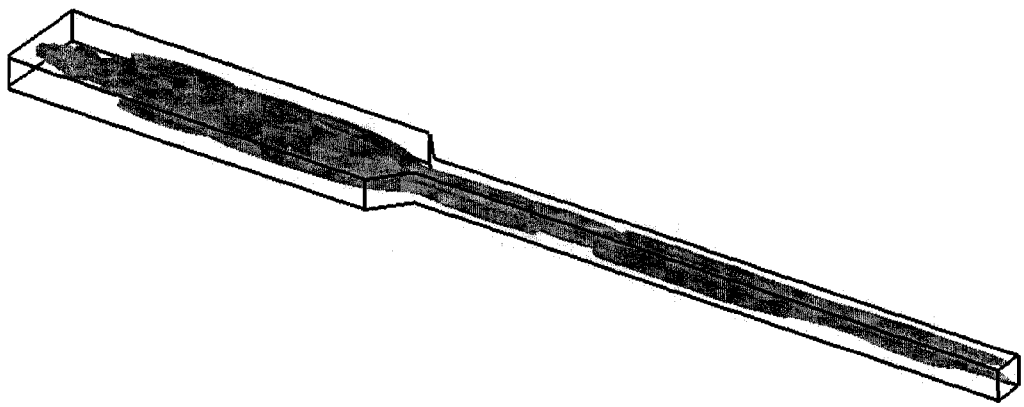

b) GLR 0.5%

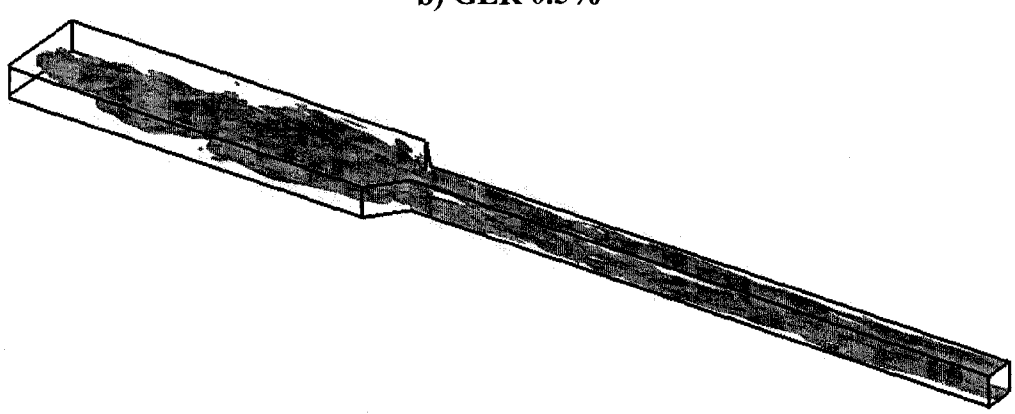

c) GLR 1.25%

Figure 3-1 Iso-surface of gas-phase volume fraction of 0.5

Figure 3-2 shows the mass flow rates of liquid at the inlet and outlet of the nozzle at the computational cycles for the GLR of 0.08%. In the initial condition, the liquid has no velocity and the outlet mass flow rate starts form zero. In order to calculate the liquid

mass flow rate at the outlet, the mass weighted flow rate of the liquid is determined based on the convection of liquid volume fraction multiplied by density through the exit surface of the nozzle. This is obtained by integrating the dot product of the flow velocity and the surface unit normal multiplied by the liquid volume fraction and density.

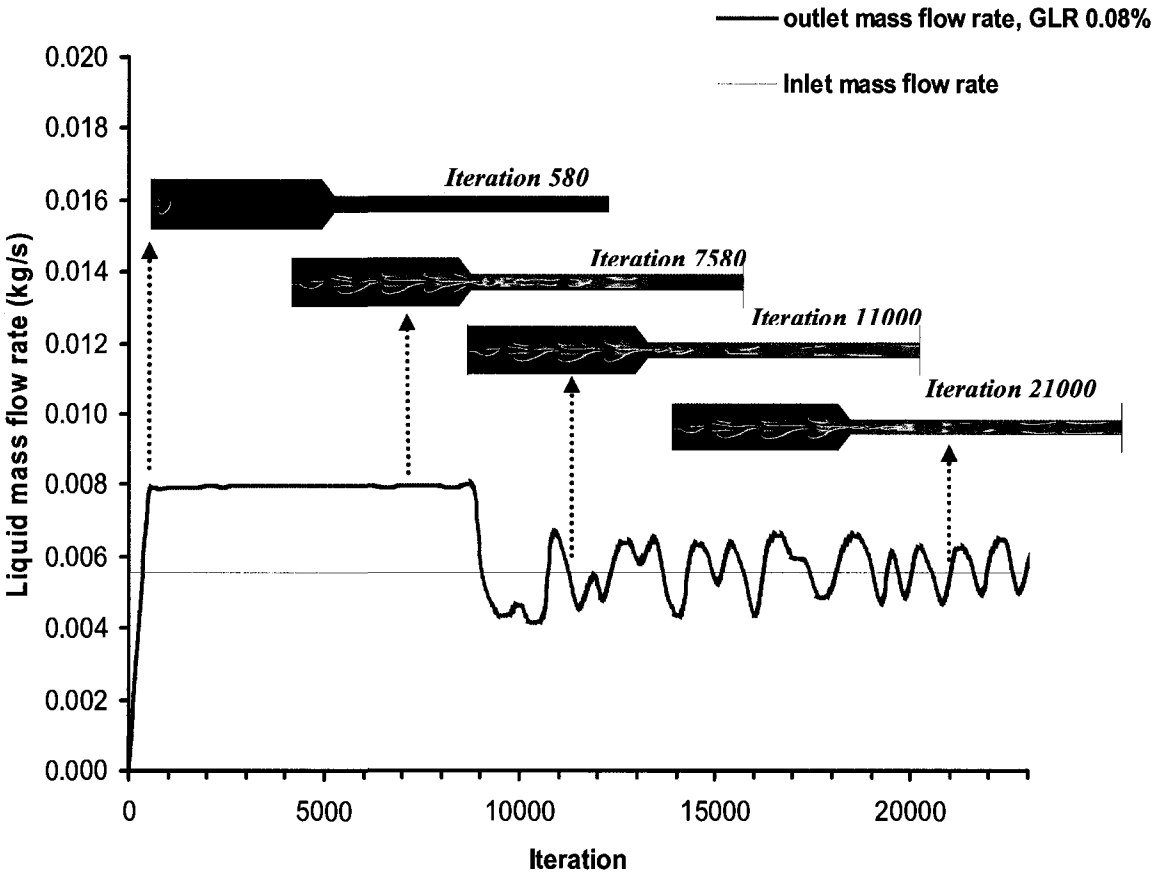

Figure 3-2 Mass flow rates of liquid at the inlet and outlet at GLR 0.08%

From the figure, since the liquid inside the nozzle has no velocity at initial time, the outlet mass flow rate starts with zero. Within the first iterations, the liquid flow is significantly accelerated and the liquid mass flow rate at the exit, suddenly increases compared to its

value at the inlet. This implies that the gas flow is entering to the mixing chamber and it displaces the liquid inside the nozzle. As the effective volume occupied by the liquid decreases, the average velocity of liquid initially increases and exhibit an initial increase in liquid mass flow rate exiting the injector. Up to about 8000 iterations, the liquid mass flow rate remains at almost constant value. During this period, the gas flow entered the domain is developed towards the mixing chamber and reaching the discharge orifice. After 8000 iterations, there is a remarkable drop in the liquid mass flow rate. This indicates that the gas flow has reached the end of the discharge passage and occupied some portion of the exit orifice. As time advances, the amplitude of the oscillation becomes smaller and eventually the outlet mass flow rate of liquid oscillates about the liquid inlet mass flow rate. These oscillations remain bounded within almost constant amplitude. It can be inferred that the internal flow may reach a statistically stationary state. All of the averaged variables are obtained after the flow reaches to this stage.

Figure 3-2 also shows the evolution of gas-phase volume fraction through the nozzle at various computational times. At the low GLR of 0.08%, the gas flow is in the form of separated bubbles generated inside the mixing chamber and evolved on their way toward the discharge passage. As the bubbles pass through the converging section, they shrink to thinner parts gradually and afterwards start to break up in the discharge passage. Due to the low aerating gas flow rate, there is no effective mixing between the liquid and gas phases in the mixing chamber and the aerating gas is still surrounded by liquid. Accordingly, the gas bubbles do not have enough inertia to mix with the liquid and accelerate it to the high velocities. In the discharge passage, the gas stream is not continuous and instead, the slug flow pattern is developed towards the end of the

discharge passage. This flow regime was observed by Lin et al. [27]. In their work, they reported the spray with large irregular droplets as the result of the operating condition.

As the aeration level is raised to a GLR of 0.15, as shown in Figure 3-3, the initial rise in liquid mass flow rate becomes more significant and within a smaller number of iterations, the mass flow rates experiences an abrupt drop. This can be related to the higher gas flow rate that pushes the liquid more towards the outlet and reaches the discharge orifice sooner than in the case with lower GLR. The outlet mass flow rate fluctuations are also noticeable at GLR of 0.15% and the outlet mass flow oscillates at larger amplitude compared to the case with GLR of 0.08%.

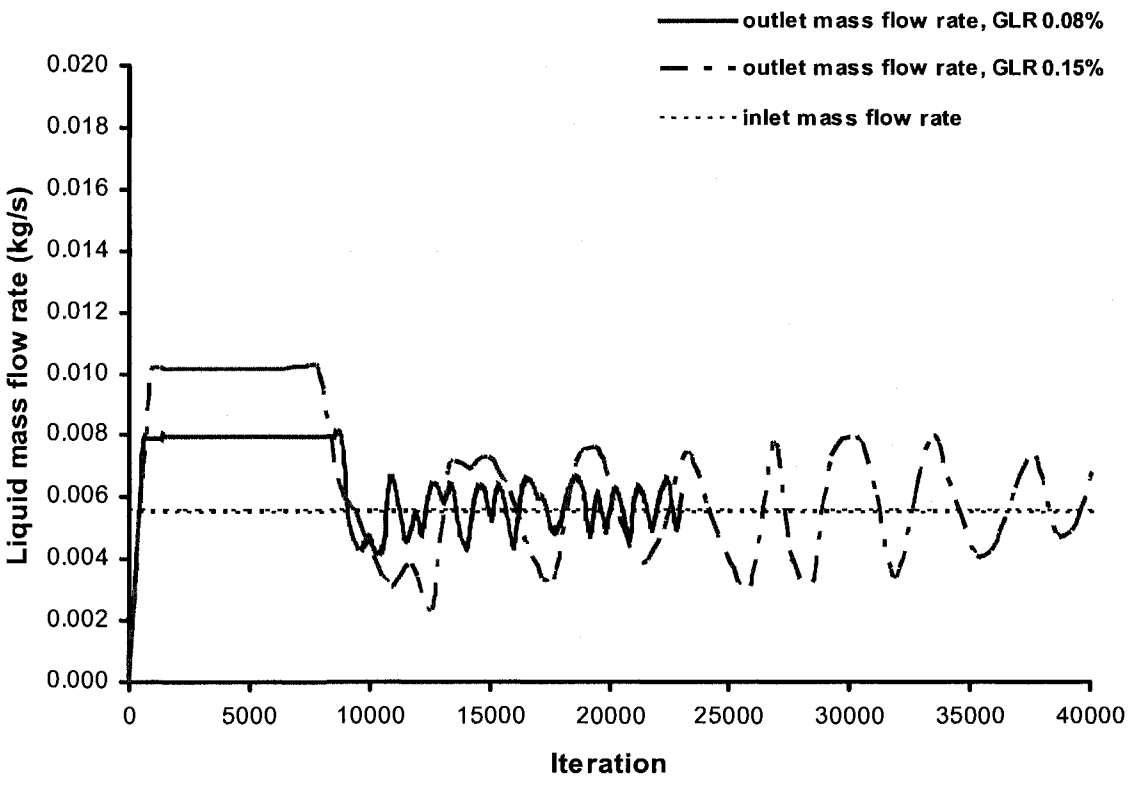

Figure 3-3 Mass flow rates of liquid at the inlet and outlet

Figure 3-4 illustrates the formation and development of gas flow volume fraction at a GLR of 0.15%. At this GLR, the bubbles grow to larger sizes and consequently larger slugs of gas are generated in the discharge passage. As shown in the figure, there are slugs of liquid in the center part of the tube following the gas slugs. This causes the flow to exhibit the fluctuating behavior at the exit of the discharge passage.

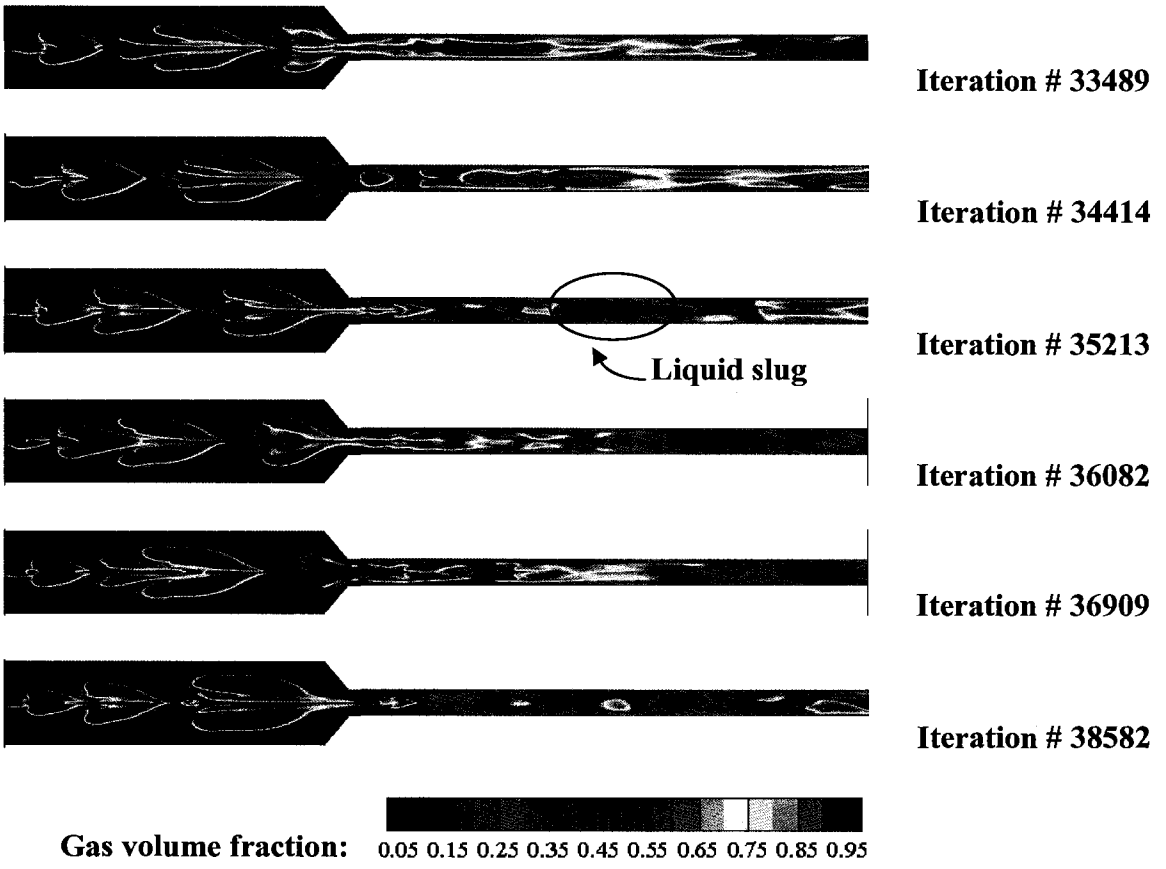

Figure 3-4 Gas-phase volume fraction contours for GLR=0.15%
(in *x-y* plane of symmetry)

By increasing the GLR to 0.5% (Figure 3-4), due to increased gas flow rate, instead of individual bubbles, large lumps of gas are formed near the end of the mixing chamber. When these gas lumps reach the converging part, they break and form slug flow pattern

around the entrance region of the discharge passage. Consequently, these slugs are conveyed to the end of the passage. At this level of aeration, the mixing between the liquid and gas flow is enhanced in the discharge passage. Lin et al [27], for GLRs of around 0.3%, reported that the structure of the resulting spray exhibits a slightly larger jet diameter.

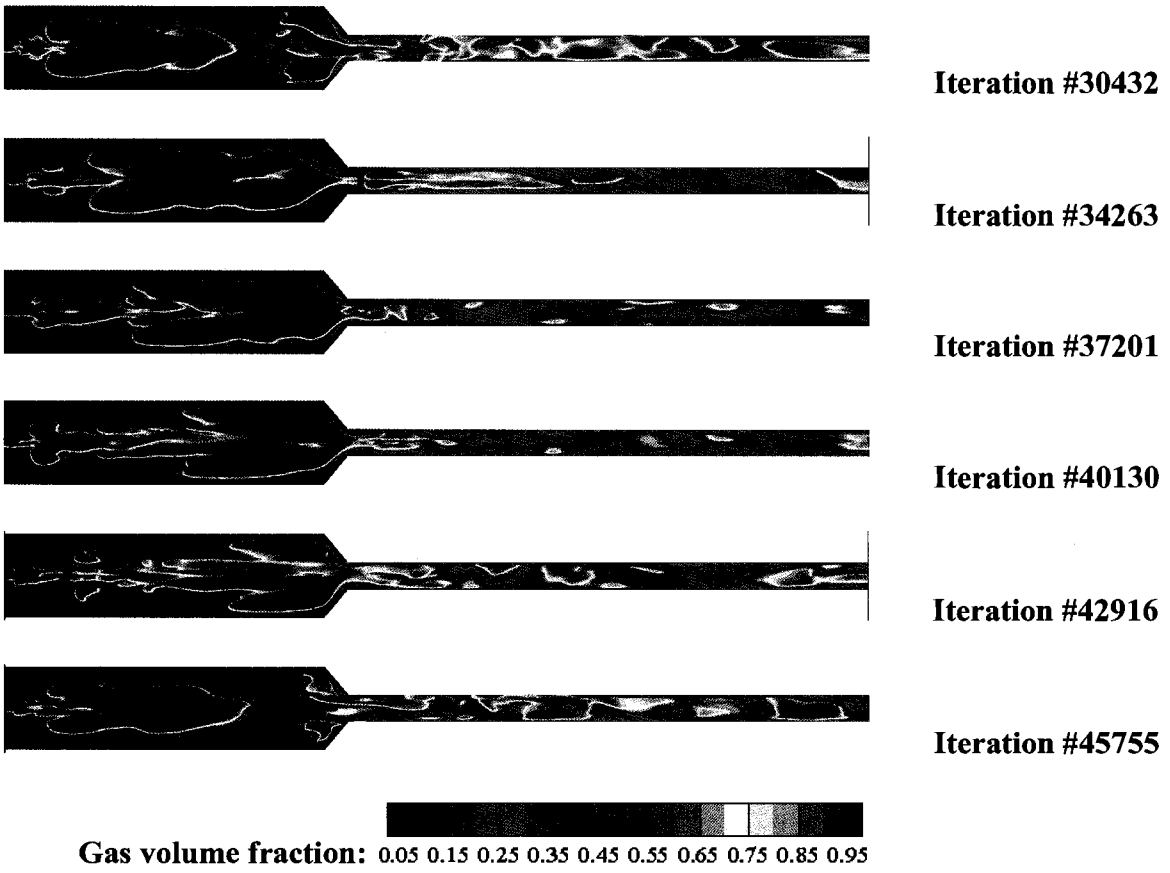

Figure 3-5 Gas-phase volume fraction contours for GLR=0.5%
(in *x-y* plane of symmetry)

With further increase in GLR to 1.25%, as shown in Figure 3-6, the liquid-gas mixing is augmented and a significant portion of the mixing chamber is filled with the aerating gas. The liquid consequently is squeezed into a thin film attached to the walls of the mixing

chamber. The two-phase flow near the exit of the discharge passage gradually developed into a co-annular flow pattern, where the core region of the passage is mainly occupied by the gas phase and a thin layer of liquid film is attached to the walls. At this GLR, the type of spray observed by Lin et al. [27] consisted of a thin liquid film with the bulk of aerating gas enclosed within the liquid and some small bubbles embedded inside the liquid film. At this level of aeration the gas flow has enough energy to break the liquid into small droplets. Hence, the produced spray can be more uniform and stable compared to the previous cases with lower GLRs.

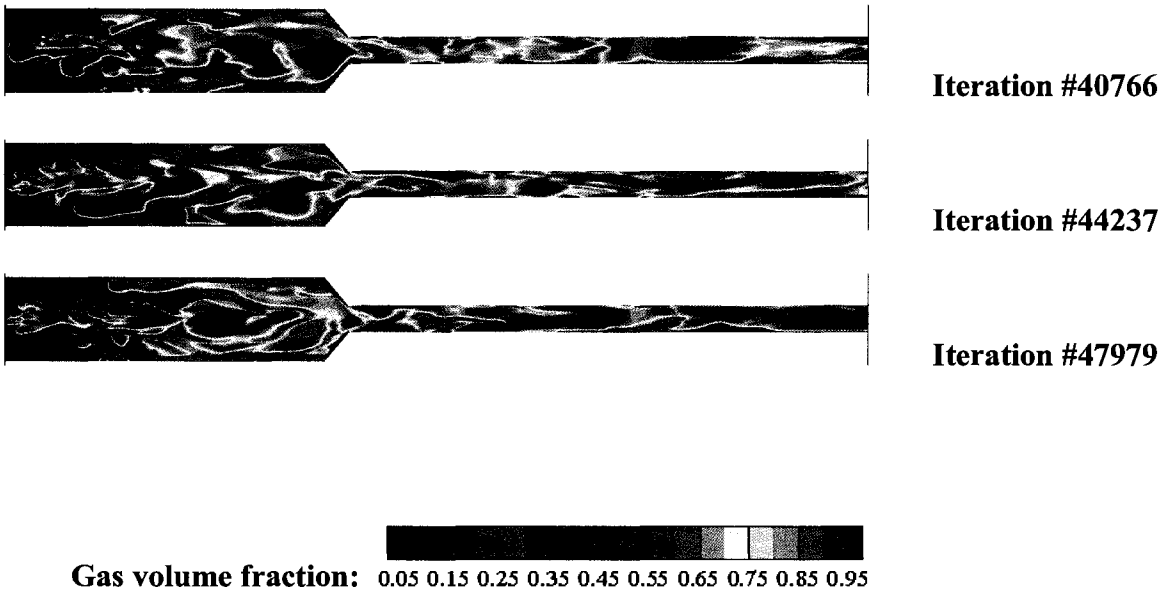

Figure 3-6 Gas-phase volume fraction contours for GLR=1.25%
(in *x-y* plane of symmetry)

3.1.1 Effect of GLR on Liquid Film Thickness

The thickness of the liquid film created in the nozzle passage greatly affects the quality of the resulting spray. For a given liquid flow rate, a thinner liquid film can produce smaller

droplets and higher velocities. In this section, the effect of different aeration levels on the liquid thickness is numerically investigated and the results are compared with the experimental data presented in the literature [27].

For the calculations of the liquid film thickness in the numerical simulations, it is assumed that the aerating gas flows inside a passage with a diameter of D_g surrounded by an annular liquid flow of thickness *h* which is obtained from the following relation;

$$h = \frac{1}{2}\left(D_H - D_g\right) \tag{3.1}$$

D_H is defined as the hydraulic diameter of the discharge passage and is 2 mm for the present geometry. D_g is calculated from the total averaged gas-volume fraction on the exit cross-section, $\bar{\alpha}_g$, and the discharge passage hydraulic diameter, D_H;

$$D_g = D_H\sqrt{\bar{\alpha}_g} \tag{3.2}$$

Once the amplitude of liquid mass flow rate's oscillations is bounded within constant values, the volume fraction contours of gas-phase are extracted. The process of computing $\bar{\alpha}_g$ can be summarized as follows; the area-averaged integration of gas-phase volume fraction $\left(\overline{\alpha_g}^{Area}\right)^t$ is taken over the nozzle discharge area at each time level *t*;

$$\left(\overline{\alpha_g}^{Area}\right)^t = \frac{\iint_{exitArea} \alpha_g^t dA}{A_{exit}} \tag{3.3}$$

The averaging process is repeated over 30 output files within 1 *msec* apart, and finally the total averaged gas-volume fraction, $\bar{\alpha}_g$, is obtained by averaging the total 30 values of $\left(\overline{\alpha_g}^{Area}\right)^t$;

$$\bar{\alpha}_g = \frac{\sum_{i=1}^{n}\left(\overline{\alpha_g}^{Area}\right)^{t_i}}{n} \quad , \quad n=30 \tag{3.4}$$

Figure 3-7 shows the numerically calculated liquid film thickness, h, by varying the aeration level; GLR 0.08% to 1.8%. The results were compared with the experimental data of Lin et al. [27]. In their experiments, in order to determine the liquid film thickness, they also assumed a cylindrical passage for the gas flow and did the measurements of the liquid film thickness over one hundred individual shadowgraph images. Based on the experimental measurements, they found a correlation between the liquid film thickness and the aerating gas flow rate which is shown on the Figure 3-7. Based on the experimental results, the thickness of the liquid film can be obtained from the gas volumetric flow rate (Q_g), which has been expressed as the ratio of GLR, liquid volumetric flow rate (Q_l), and liquid density (ρ_l), to the density of aerating gas (ρ_g), on the figure. As can be seen in Figure 3-7, the liquid film thickness in both experimental and numerical studies follows nearly the same trend, which indicates the significant role of aerating level on the thickness of the liquid film emerging from the injector. Based on the numerical results, at relatively low GLRs, an increase in the aeration level has more significant influence on the liquid film thickness compared to that at higher GLRs. The thickness of the liquid film decreases rapidly at low GLRs and then varies only slightly at high GLRs. For instance, by 0.18% increase in GLR from 0.15% to 0.33%, the liquid film

thickness decreases 42.5% from 0.40 mm to 0.23 mm. While, when the GLR increases from 1.25% to 1.8% (0.55% increase), the variation in liquid film thickness is only 13% from 0.14 mm to 0.12 mm. This indicates that increasing the amount of aerating gas up to a certain amount _which is about 1.25% in this study _can have a contribution in the thickness of the liquid film emerging from the nozzle. Therefore, any further increase in the amount of aerating gas may not have a significant effect on the liquid film thickness.

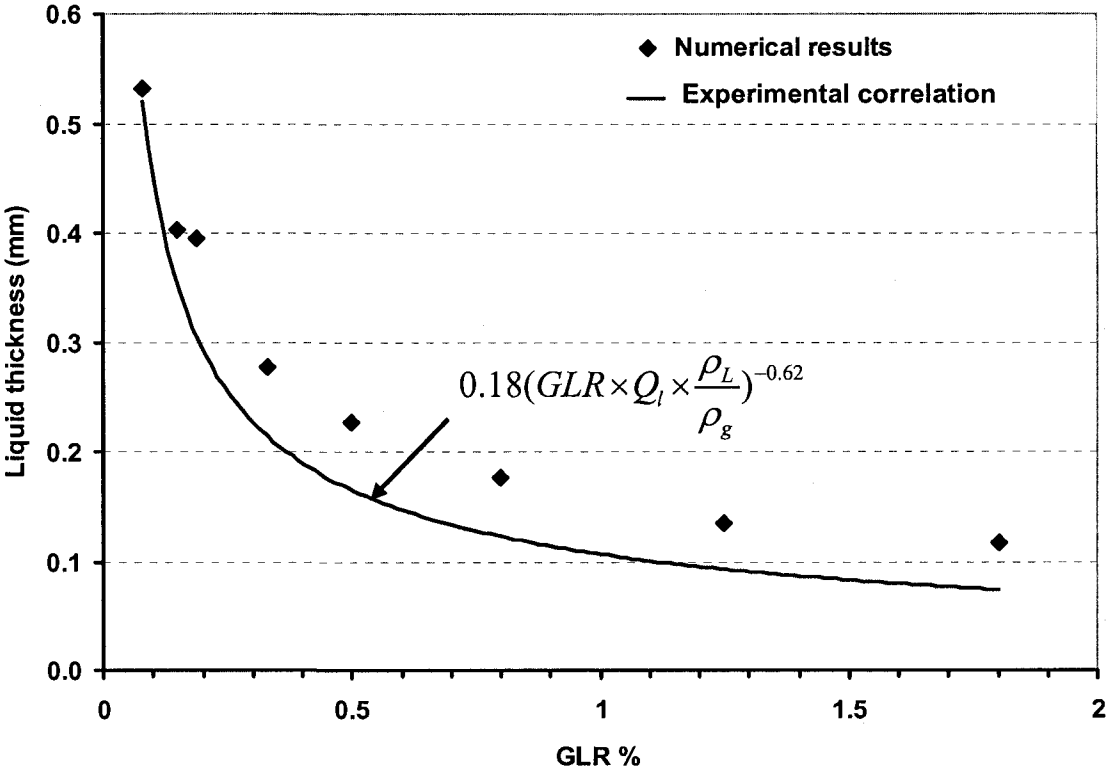

Figure 3-7 Thickness of the liquid film at various aeration levels compared with measured thickness by Lin et al. (2001)

In several applications such as the one in suspension plasma spraying, it is favorable to produce a spray with droplets as small as possible. The reason is that, upon injection, the

larger droplets with normally higher number density of suspended nanoparticles, evaporate in plasma field and result the nanoparticles agglomerate and form micron-sized particles, which will adversely affect the coating characteristics. However, having smaller droplets reduces the chance of particle agglomeration and hence helps to preserve the condition of coating with nanoparticles. Therefore, in order to reach finer sprayed droplets, the goal is to generate a thin liquid film at the nozzle exit. For the aerated-liquid jets, the spray atomization can be improved by having a co-annular flow inside the discharge passage. Generally, the thickness of the liquid film decreases as the amount of aerating gas increases. As the amount of aerating gas increases, the liquid film becomes thinner at the nozzle exit and causes the gas to liquid velocity ratio at the nozzle exit increases. Therefore, as demonstrated in Figure 3-7, one should note that increasing the flow rate of aerating gas up to GLRs around 1.25% in this study, has a prominent influence on thinning the liquid film. Any further increase in gas flow rate does not help significantly.

3.1.2 Effect of Suspension on Liquid Film Thickness

The effect of suspension of solid particles in the atomizing liquid is accounted as the change in the liquid bulk density and viscosity as described in section 2.8. For a specific aeration level, the bulk density and viscosity of liquid are changed while the liquid mass flow rate is kept constant. Figure 3-8 shows the variations of liquid film thickness with different particle concentrations. These variations are plotted at low and high levels of aeration corresponding to GLRs of 0.08% and 1.25%, respectively. Each symbol in the figure is an average of liquid film thickness, calculated based on the method explained in section 3.1.1. At the higher aeration level (GLR 1.25%), increasing in particle

concentration, shows a slight increase in the averaged film thickness from the case with no particle suspension. For both aeration levels, the last three average values of film thickness are almost the same. Generally, the trends of liquid thickness change, for both GLRs show no significant dependency on the particle concentration. This is an interesting behavior associated with the effervescent atomizer, which results in almost unchanged spray pattern for various amounts of solid concentrations in the liquid.

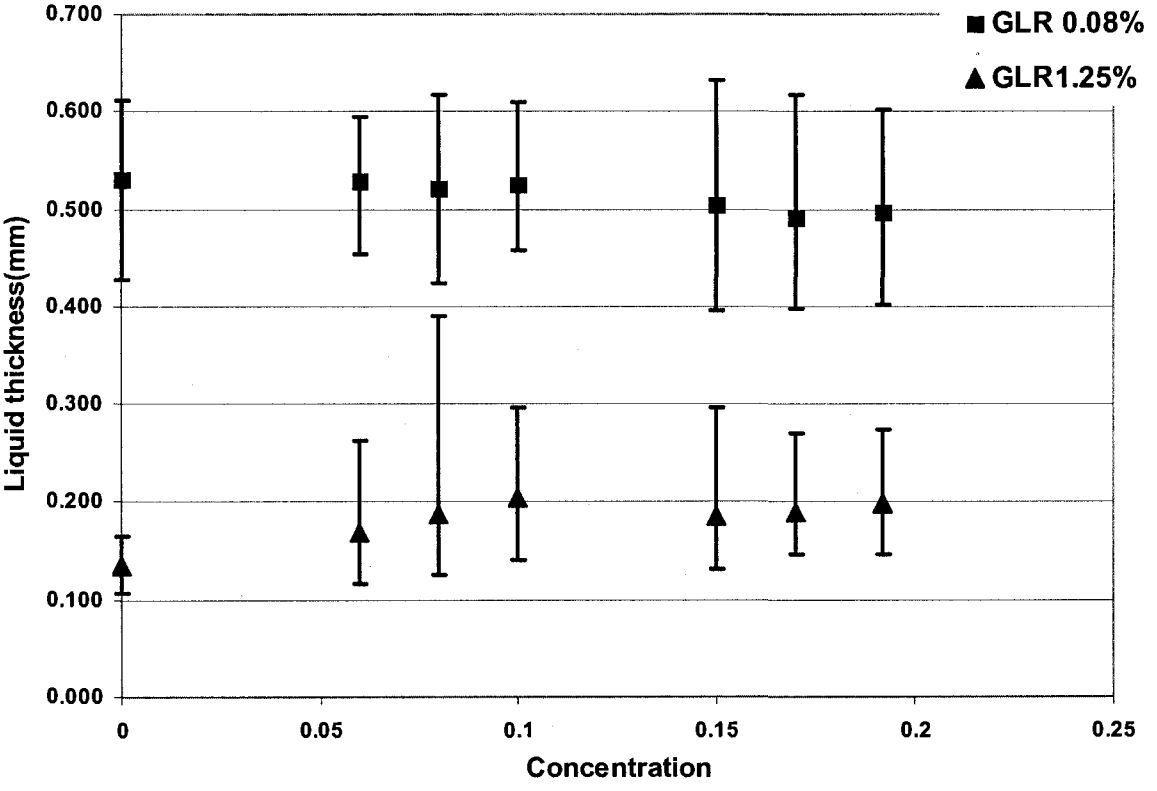

Figure 3-8 Variation of liquid film thickness with concentration

4. Conclusions and Future Work

4.1 Conclusions

In this study, a three dimensional analysis of the two-phase flow inside an effervescent atomizer was conducted. For this purpose, the Eulerian-Eulerian, two-fluid model was used to simulate the internal two-fluid liquid-gas flow in an effervescent nozzle. Different gas- to-liquid mass flow ratios were considered to study the effect of the aeration level on the internal flow structure. At low GLRs in the range of 0.08%-0.15%, the 3D iso-surfaces of gas phase revealed that the gas flow is in the form of separated bubbles generated inside the mixing chamber, and evolved on their way toward the discharge passage. At this level of aeration, no effective mixing was observed between the liquid and aerating gas in the mixing chamber. By increasing the aeration level, the mixing between the gas and liquid is enhanced and the flow structure near the nozzle exit will be changed from slug flow to co-annular flow. At this flow regime, it is expected to have more uniform and stable spray compared to the cases with lower GLRs.

It is shown that the flow rate of the aerating gas can change the liquid film thickness. Higher gas volume flow rates decrease the liquid film thickness emerging from the nozzle discharge passage. The reason is by increasing the amount of aerating gas, the volume fraction of gas phase inside the two-phase mixture increases and consequently squeezes the liquid into a thinner film.

Based on the numerical and experimental results for the variation of liquid film thickness at the injector exit for different aeration levels, it was found that at low GLRs, an increase in the aeration level has more significant influence on the liquid film thickness compared to that at higher GLRs. At low GLRs of 0.15%, the thickness of the liquid film decreases rapidly and afterward the liquid film thickness dependency on GLR reduces as GLR increases to 1.25% and finally, the liquid thickness remains within the range of 0.12-0.14 mm.

Furthermore, it was noted that the liquid film thickness does not show any significant change for various particle concentrations. It may be due to the fact that the effervescent atomizers can operate independent of liquid physical properties such as density and viscosity which is of interest in many industrial applications dealing with liquids with large varieties of viscosity.

4.2 Future Work

This work can be considered as a preliminary study in 3D numerical simulation of the complex two-phase flow regimes inside a typical effervescent atomizer. There are several areas for extension of the current work.

The drag force in this study has been modeled by the assumption of a single sphere drag model. A more comprehensive model which considers the various physical aspects such as the bubble deformation and coalescence would result in more realistic simulations. Moreover, in the current work, only the laminar flow regime was considered. In reality, the flow may exhibit turbulent behavior, especially at the higher GLR values. Hence, in future, inclusion a proper turbulence model will help to gain more realistic results in simulations with higher Reynolds number.

In order to get a better insight of the flow inside an effervescent atomizer, more experimental works are needed to be performed, to study the effect of various liquid and gas physical properties as well as the different geometry configurations on the flow structure.

Finally, in the present simulations, only the two-phase flow inside the aerated-liquid injector was investigated. In order to understand the mechanisms that may lead to formation of smaller droplets at the exit of the nozzle, a thorough study on the corresponding spray area outside of the effervescent atomizer is needed be conducted.

References

[1] Ibrahim, A. (2006) "Comprehensive Study of Internal Flow Field and Linear and Nonlinear Instability of an Annular Liquid Sheet Emanating From an Atomizer", PhD Dissertation, Dept. of Mechanical Engineering, University of Cincinnati, OH, USA

[2] Petersen, F.J., Wørts, O., Schæfer, T. & Sojka, P.E. (2001) "Effervescent Atomization of Aqueous Polymer Solutions and Dispersions", *Pharm. Dev. Technol.*, Vol. 6, Issue 2, pp. 201-210

[3] Fazilleau, J., Delbos, C., Rat, V., Coudert, J.F., Fauchais, P. & Pateyron, B. (2006) "Phenomena Involved in Suspension Plasma Spraying Part 1: Suspension Injection and Behavior", *Plasma Chem Plasma Process.*, Vol. 26, No. 4, pp. 371-391

[4] Fauchais, P., Etchart-Salas, R., Delbos, C., Tognonvi, M., Rat, V., Coudert, J. F. & Chartier, T. (2007) "Suspension and Solution Plasma Spraying of Finely Structured Layers: Potential Application to SOFCs", *Journal of Physics D: Applied Physics* , Vol. 40, pp. 2394-2406

[5] Berghaus, J.O., Marple, B. & Moreau, C. (2006) "Suspension Plasma Spraying of Nanostructured WC-12Co Coatings", *J Therm Spray Technol.*, Vol. 15, No. 4, pp. 676-681

[6] Lefebvre, A.H. (1991) "Twin-Fluid Atomization: Factors Influencing Mean Drop Size", *5th Proceedings of International Conference on Liquid Atomization and Spray Systems*, pp. 49-64

[7] Wang, X.F., Chin, J.S. & Lefebvre, A.H. (1989) "Influence of Gas Injector Geometry on Atomization Performance of Aerated-Liquid Nozzles", *Int J Turbo Jet Engines*, Vol. 6, No. 3-4, pp. 271-80

[8] Chin, J.S. & Lefebvre, A.H. (1995) "A Design Procedure for Effervescent Atomizers", *J. Eng. Gas Turbines Power*, Vol. 117, No. 2, pp. 266-271

[9] Satapathy, M.R. (1997) "The Effect of Ambient Density on the Performance of an Effervescent Diesel Injector", MSc thesis, Dept. of Mechanical Engineering, Purdue University, West Lafayette, IN, USA

[10] Sovani, S.D., Chou, E., Sojka P.E., Gore, J.P., Eckerle, W.A. & Crofts, J.D. (2000) "High Pressure Effervescent Atomization: Effect of Ambient Pressure on Spray Cone Angles", *Fuel*, Vol. 80, No. 3, pp. 427-35

[11] Loebker, D. & Empie, H.J. (1997) "High Mass Flow Rate Effervescent Spraying of High Viscosity Newtonian Liquid", *Proceedings of the 10th Annual Conference on Liquid Atomization and Spray Systems*, Ottawa, ON, pp. 253-7

[12] Lefebvre, A.H., Wang, X.F. & Martin, C.A. (1988) "Spray Characteristics of Aerated-Liquid Pressure Atomizers", *AIAA J Prop Power*, Vol. 4, No. 4, pp. 293-8

[13] Lefebvre, A.H. (1988) "A Novel Method of Atomization with Potential Gas Turbine Application", *Indian Defence Sci J.*, Vol. 38, pp. 353-62

[14] Roesler, T.C. & Lefebvre, A.H. (1989) "Studies on Aerated-Liquid Atomization", *Int. J. Turbo Jet Engines*, Vol. 6, pp. 221-30

[15] Lefebvre, A.H. (1996) "Some Recent Developments in Twin-Fluid Atomization", *Part. Part. Syst. Charact.*, Vol. 13, Issue 3, pp. 205-216

[16] Sovani, S.D., Sojka, P.E. & Lefebvre, A.H. (2001) "Effervescent Atomization", *Prog. Energy Combust. Sci.*, Vol. 27, pp. 483-521

[17] Buckner, H.E. & Sojka, P.E. (1991) "Effervescent Atomization of High Viscosity Fluids. Part 1: Newtonian Liquids", *Atomization Sprays*, Vol. 1, pp. 239-52

[18] Chin, J. S. & Lefebvre, A.H. (1993) "Flow Patterns in Internal-Mixing Twin-Fluid Atomizers", *Atomization and Sprays*, Vol. 3, pp. 463-475

[19] Spedding, P.L. & Nguyen, V.T. (1980) "Regimes Maps for Air-Water Two Phase Flow", *Chem. Eng. Sci.*, Vol. 35, pp. 779-793

[20] Lörcher, M., Schmidt, F. & Mewes, D. (2005) "Effervescent Atomization of Liquids", *Atomization and Sprays*, Vol. 15, pp. 145-168

[21] Roesler, T.C. (1988) "An Experimental Study of Aerated-Liquid Atomization", PhD Dissertation, Dept. of Mechanical Engineering, Purdue University, West Lafayette, IN, USA

[22] Roesler, T.C. & Lefebvre, A.H. (1988) "Photographic Studies on Aerated-Liquid Atomization", *Combustion Fundamentals and Applications. Proceedings of the Meeting of the Central States Section of the Combustion Institute*, Indianapolis, Indiana, Paper 3

[23] Buckner, H.E., Sojka, P.E. & Lefebvre, A.H. (1990) "Effervescent Atomization of Coal-Water Slurries", *ASME Publ*, pp. 105-8

[24] Lund, M.T., Sojka, P.E., Lefebvre, A.H. & Gosselin, P.G. (1993) "Effervescent Atomization at Low Mass Flow Rates Part 1: The Influence of Surface Tension", *Atomization Sprays*, Vol. 3, pp. 77-89

[25] Lund, M.T. & Sojka, P.E. (1992) "Effervescent Atomization at Low Mass Flow Rates Part 2: The Structure of the Spray", *Proceedings of the 5th Annual Conference on Liquid Atomization and Spray Systems*, San Ramon, CA, USA, pp. 233-7

[26] Li, J., Lefebvre, A.H. & Rollbuhler, J.R. (1994) "Effervescent Atomization for Small Gas Turbines", American Society of Mechanical Engineers, 94-GT-495, pp. 1-6

[27] Lin, K.C., Kennedy, P.J. & Jackson, T.A. (2001) "Structures of Internal Flow and the Corresponding Spray for Aerated-Liquid Injectors", *AIAA Paper* 2001-3569

[28] Sutherland, J.J., Panchagnula, M.V., Sojka, P.E., Plesniak, M.W. & Gore, J.P. (1995) "Effervescent Atomization at Low Air-Liquid Ratios", *Proceedings of the 8th Annual Conference on Liquid Atomization and Spray Systems*, Troy, MI, pp. 74-7

[29] Whitlow, J.D. & Lefebvre, A.H. (1993) "Effervescent Atomizer Operation and Spray Characteristics", *Atomization and Sprays*, Vol. 3, Issue 2, pp. 137-56

[30] Bush, S.G., Bennett, J.B., Sojka, P.E., Panchagnula, M.V. & Plesniak, M.W. (1996) "Momentum Rate Probe for Use with Two-Phase Flows", *Rev Sci Instrum*, Vol. 67, pp. 1878-85

[31] Sutherland, J.J., Sojka, P.E. & Plesniak, M.W. (1997) "Entrainment by Ligament-Controlled Effervescent Atomizer-Produced Sprays", *Int J Multiphase Flow*, Vol. 23, pp. 865-84

[32] Sutherland, J.J., Sojka, P.E., Plesniak, M.W. & Gore, J.P. (1996) "Entrainment by Low Air-Liquid Ratio Effervescent Atomizer Produced Sprays", *Proceedings of the 9th Annual Conference on Liquid Atomization and Spray Systems*, San Francisco, CA, USA

[33] Panchagnula, M.V. & Sojka, P.E. (1999) "Spatial Droplet Velocity and Size Profiles in Effervescent Atomizer-Produced Sprays", *Fuel*, Vol. 78, pp. 729-41

[34] Schmidt, F. & Mewes, D. (2006) "Measuring Flow Velocity and Flow Pattern of a Suspension-Gas Mixture Inside the Twin-Fluid Atomizer", *Proc. of FEDSM, ASME Joint U.S. European Fluids Engineering Summer Meeting*, Miami, Florida, USA

[35] Bove, S. (2005) "Computational Fluid Dynamics of Gas-Liquid Flows Including Bubble Population Balances" PhD Dissertation, Aalborg University, Denmark

[36] Tian, M. (2002) "A Numerical Simulation of Internal Two-Phase Flow for Aerated-Liquid Injectors", MSc thesis, Dept. of Mechanical Engineering, North Carolina State University, NC, USA

[37] Arabzadeh, S. & Dolatabadi, A. (2007) "Numerical Simulation of Nano-Particle Suspension in an Effervescent Atomizer", accepted , *Journal of Computational and Theoretical Nanoscience*

[38] Arabzadeh, S. & Dolatabadi, A. (2007) "Suspension Spray in a Twin-Fluid Atomizer", *Proceeding of the 5th Joint ASME/JSME Fluids Engineering Conference*, July 30-Aug 2, San Diego, CA, USA

[39] Arabzadeh, S. & Dolatabadi, A. (2007) "Modeling Two-Phase Flow in Suspension Sprays", *Proceeding of the 15th Annual Conference of the CFD Society of Canada*, May 2007

[40] Drew, D.A. (1983) "Mathematical Modeling of Two-Phase Flow", *Annual Review of Fluid Mechanics*, Vol. 15, pp. 261-291

[41] Drew, D.A. & Passman, S.L. (1999) *Theory of Multicomponent Fluids*, Springer-Verlag. New York

[42] Kashiwa, B.A., Padial, N.T., Rauenzahn, R.M. & VanderHeyden, W.B. (1994) "A Cell-Centered ICE Method for Multiphase Flow Simulations", Los Alamos National Laboratory Report LA-UR-93-3922 Revised, Los Alamos, NM

[43] Comer J.K. (1998) "Computational Two-Phase Flow Analyses and Applications to Gas-Liquid and Gas-Solid Flows", PhD Dissertation, Dept. of Mechanical Engineering, North Carolina State University, NC, USA

[44] Padial, N.T., VanderHeyden, W.B., Rauenzahn, R.M. & Yarbro, S.L. (2000) "Three-Dimensional Simulation of a Three-Phase Draft-Tube Bubble Column", *Chem. Eng. Sci.* Vol. 55, pp. 3261-3273

[45] Amsden, A.A. & Harlow, F.H., (1970) "The SMAC Method: A Numerical Technique for Calculating Incompressible Fluid Flows", Los Alamos Scientific Laboratory Report LA-4370, Los Alamos, NM

[46] Gaffney E.S. & Kashiwa B.A. (2003) *Users Manual for CFDLib Version 02.1*, Los Alamos National Laboratory Report LA-UR-03-0657 , Los Alamos

[47] Thomas, D.G. (1965) "Transport Characteristics of Suspensions, 8. A Note on Viscosity of Newtonian Suspension of Uniform Spherical Particles", *Journal of Colloid Science*, Vol. 20, No. 3, pp. 267

Appendix

Definition of Average Variables

Volume Fraction $$\alpha_k = \bar{X}_k \quad \text{(a- 1)}$$

Density $$\bar{\rho}_k = \frac{\overline{X_k \rho_k}}{\alpha_k} \quad \text{(a- 2)}$$

Velocity $$\bar{\vec{v}}_k = \frac{\overline{X_k \rho_k \vec{v}_k}}{\alpha_k \bar{\rho}_k} \quad \text{(a- 3)}$$

Stress $$\bar{\bar{T}}_k = \frac{\overline{X_k \bar{\bar{T}}_k}}{\alpha_k} \quad \text{(a- 4)}$$

Reynolds Stress $$\bar{\bar{\tau}}_k^{\mathrm{Re}} = \frac{\overline{-X_k \rho_k \vec{v}_k' \vec{v}_k'}}{\alpha_k} \quad \text{(a- 5)}$$

Mass Weighted Averages [43]

Interfacial Mass,

$$\left(m_k^n\right)_i = \frac{1}{2}\left[\left(m_k^n\right)_l + \left(m_k^n\right)_r\right] \quad \text{(a- 6)}$$

Where,

$\left(m_k^n\right)_l = \left(V \alpha_k \rho_k^0\right)_l^n$ Mass in *left* control volume

$\left(m_k^n\right)_r = \left(V \alpha_k \rho_k^0\right)_r^n$ Mass in *right* control volume

Interfacial Mass Weighted Average Velocity,

$$\left\langle\left\langle \vec{v}_k^n \right\rangle\right\rangle^{\rho_k} = \frac{\left(m_k \vec{v}_k\right)_i^n}{\left(m_k^n\right)_i} = \frac{\left(m_k^n\right)_l . \vec{v}_{k,l}^n + \left(m_k^n\right)_r . \vec{v}_{k,r}^n}{\left(m_k^n\right)_l + \left(m_k^n\right)_r} \quad \text{(a- 7)}$$

Interfacial Mass Weighted Average Specific Volume,

$$\left\langle\left\langle \vartheta_k^0 \right\rangle\right\rangle^{\rho_k} = \frac{\left(\alpha_k V\right)_i^n}{\left(m_k^n\right)_i} = \frac{\left(v_k^0\left(\alpha_k \rho_k^0\right)V\right)_i^n}{\left(m_k^n\right)_i} = \frac{\left(m_k^n\right)_l . v_{k,l}^0 + \left(m_k^n\right)_r . v_{k,r}^0}{\left(m_k^n\right)_l + \left(m_k^n\right)_r} \qquad \text{(a- 8)}$$

Interfacial Mass Weighted Average Momentum Exchange Coefficient,

$$\left\langle\left\langle v_k^0 \alpha_l K_{kl} \right\rangle\right\rangle^{\rho_k} = \frac{\left(\alpha_k \alpha_l V K_{kl}\right)_i^n}{\left(m_k^n\right)_i} = \frac{\left(v_k^0\left(\alpha_k \rho_k^0\right)V\right)_i^n}{\left(m_k^n\right)_i} = \frac{\left(m_k^n\right)_l . \left(v_k^0 \alpha_k K_{kl}\right)_l + \left(m_k^n\right)_r . \left(v_k^0 \alpha_k K_{kl}\right)_l}{\left(m_k^n\right)_l + \left(m_k^n\right)_r} \qquad \text{(a- 9)}$$